



GLAST Tracker Static and Dynamic Analysis

Franz Biehl
4/31/2001

	Name:	Phone & E-Mail	Signature:
Main Author:	Franz Biehl	1-505-661-3000 biehl@hytecinc.com	
Approved:	Erik Swensen	1-505-661-4021 swensen@hytecinc.com	

Abstract

This report documents the static, dynamic, and thermal finite element model analysis of the GLAST tracker tower assembly. Detailed individual trays representing the five distinct tray configurations consisting of the bottom, standard no-payload, superglast, standard, and top tray are analyzed. Results are given for tower models that simulate a rigid base attachment, flexure mounted attachment, and flexure attachment with non-bonded corner closeout assemblies. Trays are simulated with detailed closeouts, cores, face sheets, and payloads.

Results are tabulated and plotted for modal frequencies, random vibration response, and static acceleration loads. Individual tray and overall tower analysis results are presented. Corner loads are calculated for acceleration loads to permit an estimate of the non-connect closeouts viability.

DESIGN ENGINEERING
ADVANCED COMPOSITE APPLICATIONS
ULTRA-STABLE PLATFORMS

110 EASTGATE DR.
LOS ALAMOS, NM 87544

PHONE 505 661-3000
FAX 505 662-5179
WWW.HYTECINC.COM



Revision Log

Rev.	Date	Author(s)	Summary of Revisions/Comments
-	June 4, 2001	Franz Biehl	Initial release.

Table of Contents

1. Summary	4
2. Finite Element Model Description	4
2.1 Geometry and elements	4
2.1.1 Tray models	4
2.1.2 Detailed tracker tower model	7
2.1.3 Simplified tracker model	9
2.2 Material properties	10
2.2.1 Closeout frame	10
2.2.2 Face sheets	11
2.2.3 Core	12
2.2.4 Sidewalls	13
2.2.5 Flexures and screws	14
2.3 Boundary conditions	14
2.3.1 Tray models	14
2.3.2 Tower models	14
3. Analysis Results	14
3.1 Modal analysis	14
3.1.1 Tray models	14
3.1.2 Detailed tower model	16
3.2 Random vibration analysis	22
3.2.1 Input spectrum	22
3.2.2 Single tray response	22
3.2.3 Tower response	25
3.3 Static analysis	26
3.3.1 Static acceleration loads	26
3.3.2 Base tray corner closeout loads (flexure mount configuration)	33
3.3.3 Assembly distortion	36
3.3.4 Grid deformation induced stress	37
3.4 Thermal analysis	38
4. Conductive Elastomer and Closeout Frame Redesign	40
4.1 Tracker frequencies	40
4.2 Random response	41
4.3 Static loads	41
4.4 Thermal analysis	43
5. Summary and Conclusions	44
6. References	44
Appendix A: Closed-Form Modal Frequency Calculations	45
Appendix B: Closed-Form Calculation of Single-mode Random Vibration Response	46

1. Summary

This document summarizes finite element model (FEM) and closed form analysis results for the GLAST tracker assembly. Results reported include single tray and overall tracker tower response to static acceleration loads and random vibration inputs; and resonant vibration modes. Tables listing material, lamina, and laminate properties are included. Calculated responses listing stresses and displacements are tabulated for specific structural locations of interest. The effects of two support conditions are examined as well as the effect of closeout frame corner integrity. Closed form results are compared with the FEM results to confirm the FEM calculations. Probability of tray mid-panel contact between adjacent trays is calculated for the random environment.

2. Finite Element Model Description

The COSMOS^[1] finite element code is used to generate finite element structural models (FEM), calculate normal vibration modes, response to static acceleration loads and the response to a random vibration input spectrum. Three dimensional solid elements; as well as two dimensional shell elements, are used to simulate the tray closeout structures. Solid elements are used to represent the honeycomb core and some parts of the flexure mount structures. Tray face sheets and tracker sidewalls are simulated using laminated shell elements. Individual tray assemblies are simulated as well as a complete tracker tower assembly.

Two tracker support configurations are modeled. The configuration simulates a fixed (all six degrees-of-freedom) constraint at the bottom of the bottom (lowest) tray and the second configuration simulates discreet flexures mounted to bottom tray. In addition, a gap at the closeout tray corners is modeled in the flexure mount support design in order to study the effect of using a discontinuous closeout frame (i.e. corners are not bonded together).

2.1 Geometry and elements

2.1.1 Tray models

An overall view of the closeout frame finite element representation is shown in Figure 1 and a close up view of a corner section appears in Figure 2. Members shown in green and red are solid elements while those in blue are shell elements. A modified tray is used for the bottom and top trays, as shown in Figure 3.

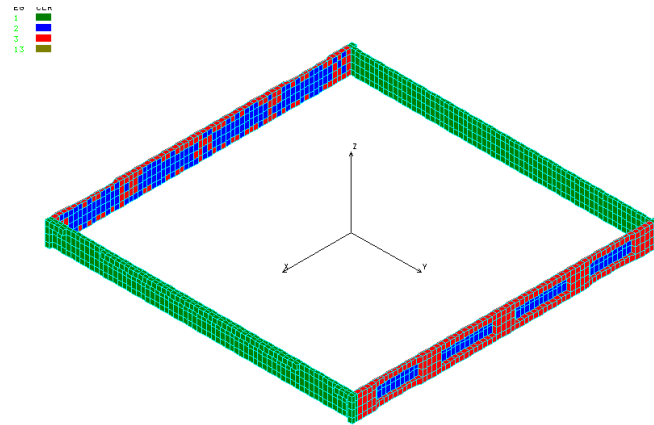


Figure 1: Closeout frame FEM.

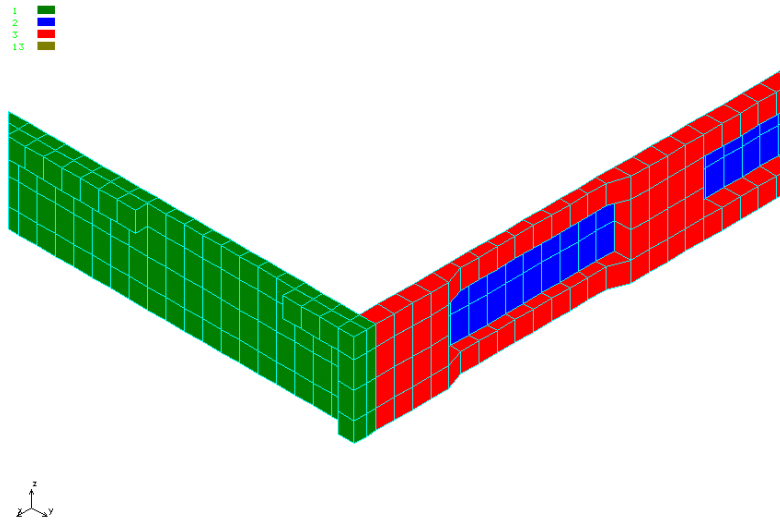


Figure 2: Close up view of closeout frame FEM.

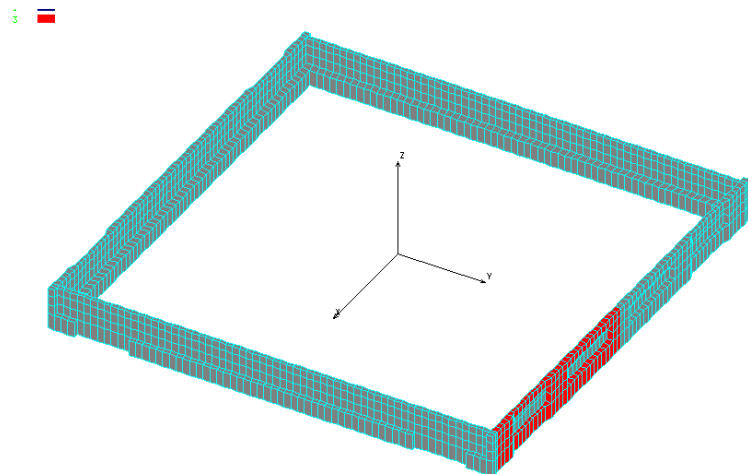


Figure 3: Base and top tray closeout model.

The interior closeout frame volume is filled with solid elements to represent the honeycomb core and this volume is covered on both sides by layered shell elements that reflect the face sheet plus payload properties. Figure 4 shows the complete tray FEM with closeout frame, core, and face sheets.

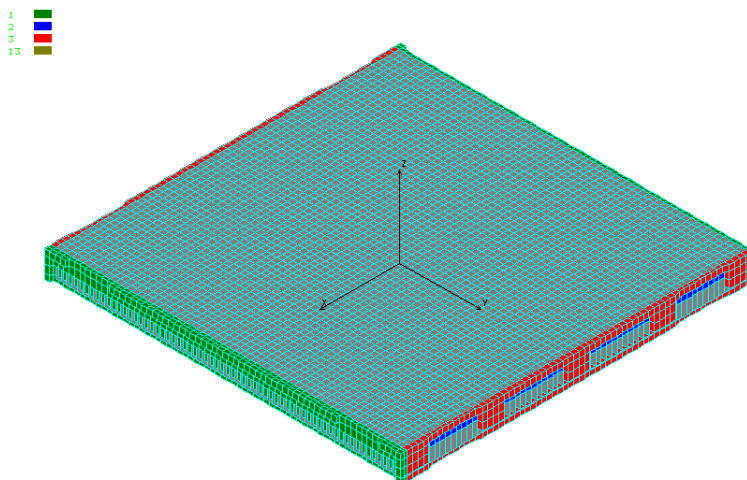


Figure 4: Detailed tray FEM.

Five individual detailed tray finite element models are required to simulate the five tray configurations. Layers for a standard upper payload are listed in Table 1 in a direction away from the face sheet. Copper layer densities are multiplied by a factor that estimates the effective amount of surface area for the individual copper layer.

Table 1: Upper payload layers simulated in a standard upper structure above face sheet.

Material	Thickness (μm)	Density (kg/m^3)
Silicon detector	400	2330
Silicon adhesive	75	1430
Copper sheet	16.5	8940 * 10%
Aramid	200	1250
Copper sheet	16.5	8940 * 50%
Epoxy adhesive	75	2450
Face sheet layers		

Lower surface payload layers are displayed in Table 2. Layers are listed from the face sheet and downward showing the subsequent layers. A density factor is again applied to the tungsten layer to account for gaps between the tungsten segments. Two values are shown for the tungsten converter, the first is for the standard tray and the second is for the superglast tray.

Table 2: Lower payload layers simulated in a standard structure below the face sheet (two values for tungsten refer to the standard and superglast tray).

Material	Thickness (μm)	Density (kg/m ³)
Face sheet layers		
Epoxy adhesive	75	2450
Aramid	152	1250
Tungsten	105 and 630	19300 * 95%
Copper sheet	16.5	8940 * 50%
Aramid	200	1250
Copper sheet	16.5	8940 * 10%
Silicon adhesive	75	1430
Silicon detector	400	2330

Finally, the five tray simulations are tabulated in Table 3 in regard to the core, face sheet, and upper and lower payload configurations. Core and face sheet layer details are provided in a subsequent section concerning materials.

Table 3: Tray configurations showing core, face sheet, and payload descriptions used in FEM models.

Tray	Core	Face sheet	Upper payload	Lower payload
base	standard	standard	standard upper	none
bottom	standard	standard	standard upper	standard upper
superglast	superglast	standard	standard upper	superglast lower
standard	standard	standard	standard upper	standard lower
top	standard	standard	none	standard lower

2.1.2 Detailed tracker tower model

The detailed tracker tower model consists of individual trays (19), sidewalls, and a flexure support system. Tray models are slightly simplified versions of the detailed tray models described in a previous section. Again the trays are simulated by layered shell elements representing the core, face sheet, and payload characteristics plus solid elements representing the closeout structure. These trays differ from the detailed trays only in the number of elements representing the core and face sheet plus payload simulation. Modal analysis of each tray configuration showed a very slight change (less than one percent) in first mode frequency compared with the detailed tray models.

Beam elements are used to represent each of the assembly fasteners connecting the sidewalls to the trays. The sidewalls are simulated by layered shell elements and are the only structural elements that bind the entire stack together. There are no direct connectors between individual tray closeout structures. Figure 5 shows a typical tray finite element model used in the detailed tower assembly.

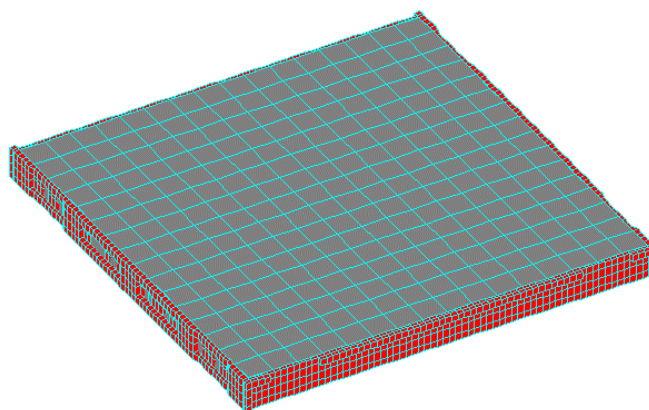


Figure 5: Typical tray FEM used in detailed tracker tower model showing shell and beam elements (19 of these in assembly).

Figure 6 depicts the sidewalls and the top tray closeout used in the tracker tower model. Nineteen trays are attached to the sidewalls via screws simulated by beam elements. The base tray and top trays use modified tray closeouts that incorporate a boss along the inner surface that is to be used for base mounting or for attaching a lifting fixture as shown in Figure 6.

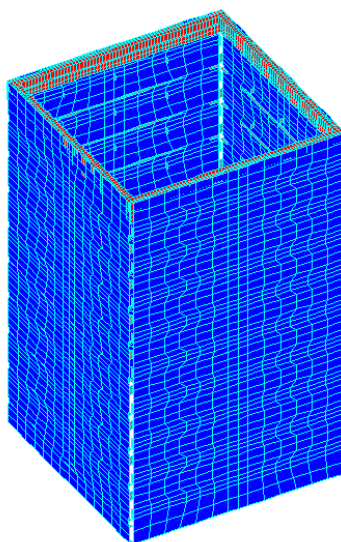


Figure 6: Detailed tracker FEM showing sidewalls and top tray closeout.

A close up view of the tracker tower FEM appears in Figure 7, while the individual tray elements are shown systematically (single layer to represent a tray) without the sidewalls in Figure 8. The various colors used in Figure 8 symbolize the five different tray types where dark green is the bottom tray (1 tray), light blue denotes the 2 standard no-payload trays, red denotes the 4 superglast trays, light green the 11 standard trays, and dark blue the top tray.

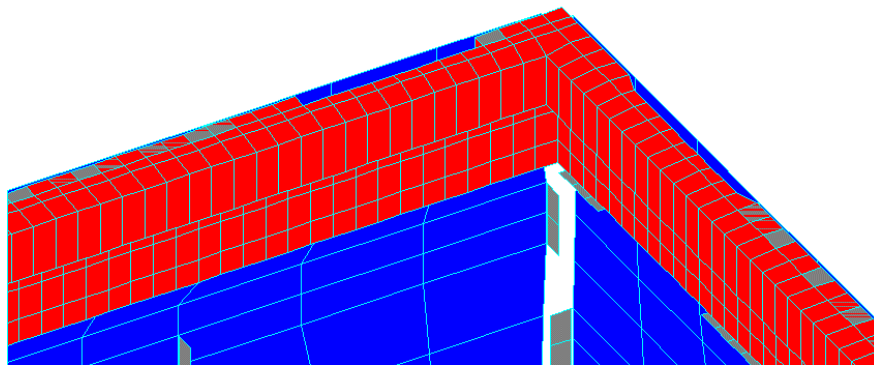


Figure 7: Close up view of top tray closeout and sidewall of detailed tracker tower FEM.

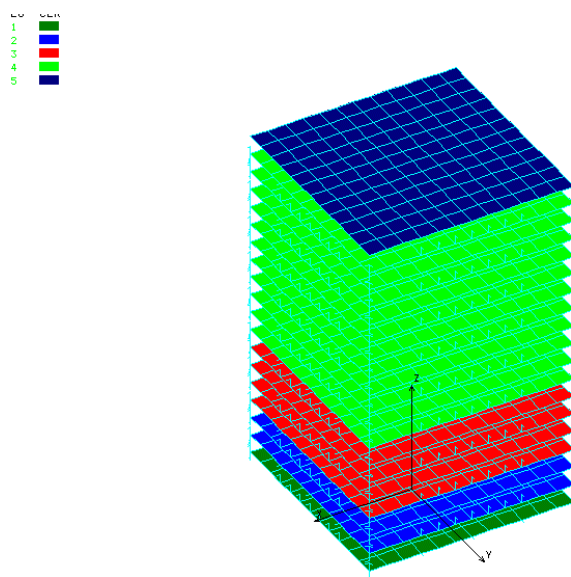


Figure 8: Schematic view of tray stack that illustrates tray sequence (trays shown as single layers).

2.1.3 Simplified tracker model

Simplified tracker models are generated for use in a subsequent comprehensive instrument FEM. Sixteen identical towers are used in the instrument model. These simplified models are necessary to ensure that the instrument model degree of complexity is reasonable. To ensure that these models are representative of the detailed tower tracker models, it is desirable that these models represent the individual tray type mass and first mode frequency. This is achieved by “tuning” the tray isotropic panel models that replace the detailed tray models by adjusting the material stiffness while holding the total mass constant. These individual trays representing the different tray types are assembled in a stack that is supported by the orthotropic sidewalls. The base tray is attached to the tower support flexure mounts. Figure 9 is a view of a tray FEM used in the simple tracker model and Figure 10 displays the simple tracker FEM.

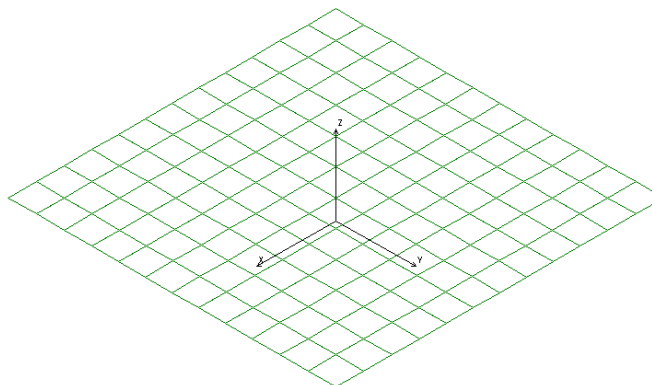


Figure 9: Typical tray model used in simple tracker tower model.

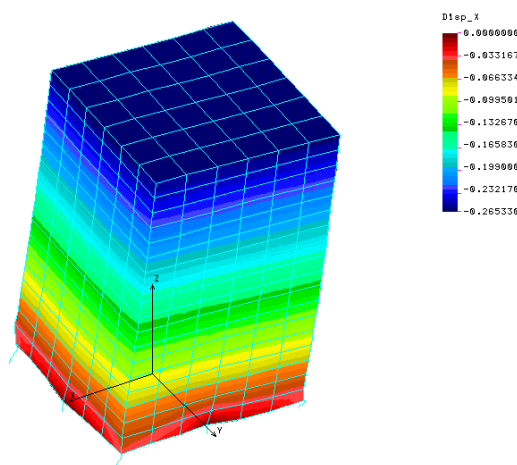


Figure 10: Simple tracker model.

2.2 Material properties

Material properties for the various components simulated in the FEM are presented in the sections that follow. In general, composite material property values ^{[2],[3]} are taken from vendor test data and/or from properties calculated for composite structural materials. In some cases, specific information is considered proprietary so that the source cannot be revealed. Standard tables of properties are used for the homogeneous materials such as aluminum, steel, and titanium.

Face sheet composite materials tested lower property values than expected and these properties are used in assessing the impact upon tray performance.

2.2.1 Closeout frame

The closeout frame is fabricated from Resin-Impregnated 3D Carbon-Carbon material obtained from Allcomp Inc. Expected properties for this material are given in Table 4.

Table 4: Properties used in FEM for the closeout frame.

Structural properties		Thermal properties	
Modulus		Expansion coefficient	
E _{xx} (GPa)	35.0	CTE _{xx} (ppm/K)	0.4
E _{yy} (GPa)	35.0	CTE _{yy} (ppm/K)	0.4
E _{zz} (GPa)	3.5	CTE _{zz} (ppm/K)	4.3
Shear modulus		Heat transfer	
G _{xy} (GPa)	1.5	K _{xx} (W/mK)	204.5
G _{xz} (GPa)	16.0	K _{yy} (W/mK)	204.5
G _{yz} (GPa)	16.0	K _{zz} (W/mK)	129
Poisson ratio		Specific heat	
v _{xy}	0.1		
v _{xz}	0.3		
v _{yz}	0.3		

2.2.2 Face sheets

Face sheet lamina (YSH50 fibers and RS-3 resin) properties are listed in Table 5 and the laminate properties are given in Table 6. The first property column in each table is the computed value based upon fiber and resin properties. The second and third columns are adjusted values to match measured laminate modulus values (76.5GPa standard tray and 94.5GPa superglast).

Table 5: Face sheet theoretical lamina properties.

Structural properties				Thermal properties			
Modulus	Compute	Stand tray	Super tray	CTE	Compute	Stand tray	Super tray
E ₁₁ (GPa)	313	217	269	CTE ₁ (ppm/K)	-1.23	-0.73	-1.01
E ₂₂ (GPa)	6.1	4.9	5.6	CTE ₂ (ppm/K)	25.85	25.89	25.87
E ₃₃ (GPa)	6.1	4.9	5.6	CTE ₃ (ppm/K)	25.85	25.89	25.87
Shear modulus				Heat transfer			
G ₁₂ (GPa)	3.6	3.2	3.4	K ₁₁ (W/mK)	111.1	76.7	95.4
G ₁₃ (GPa)	3.6	3.2	3.4	K ₂₂ (W/mK)	0.59	0.59	0.59
G ₂₃ (GPa)	2.5	2.0	2.3	K ₃₃ (W/mK)	0.59	0.59	0.59
Poisson ratio				Specific heat			
v ₁₂	0.24	0.24	0.24				
v ₁₃	0.24	0.24	0.24				
v ₂₃	0.24	0.24	0.24				

Table 6: Face sheet lamina properties.

Structural properties				Thermal properties			
Modulus	Compute	Stand tray	Super tray	CTE	Compute	Stand tray	Super tray
E11 (GPa)	109.4	76.5	94.5	CTE1 (ppm/K)	-0.595	-0.038	-0.333
E22 (GPa)	109.4	76.5	94.5	CTE2 (ppm/K)	-0.595	-0.038	-0.333
E33 (GPa)	6.4	5.2	5.9	CTE3 (ppm/K)	32	30	32
Shear modulus				Heat transfer			
G12 (GPa)	41.4	29.0	35.8	K11 (W/mK)	55.8	38.6	48.01
G13 (GPa)	3.0	2.6	2.9	K22 (W/mK)	55.8	38.6	48.01
G23 (GPa)	3.0	2.6	2.9	K33 (W/mK)	0.586	0.525	0.586
Poisson ratio				Specific heat			
v12	0.322	0.317	0.320				
v13	0.183	0.184	0.183				
v23	0.183	0.184	0.183				

2.2.3 Core

A different aluminum core is used for the superglast tray versus all other tray types. Core properties are listed in Table 7. The core used in the, bottom, standard no-payload, standard, and top tray is 3/8 cell size, 5056 Al, 0.0007 wall thickness and the superglast is a 3/8 cell size, 5056 Al, 0.002 wall thickness.

Table 7: Structural and thermal properties for tray cores.

Base, bottom, standard, and top tray core				Superglast tray core			
Structural properties		Thermal properties		Structural properties		Thermal properties	
Modulus		Expansion coefficient		Modulus		Expansion coefficient	
E _{xx} (Mpa)	0.62	CTE _{xx} (ppm/K)	23.16	E _{xx} (MPa)	0.62	CTE _{xx} (ppm/K)	23.16
E _{yy} (Mpa)	0.62	CTE _{yy} (ppm/K)	23.16	E _{yy} (MPa)	0.62	CTE _{yy} (ppm/K)	23.16
E _{zz} (GPa)	0.093	CTE _{zz} (ppm/K)	23.16	E _{zz} (GPa)	0.571	CTE _{zz} (ppm/K)	23.16
Shear modulus		Heat transfer		Shear modulus		Heat transfer	
G _{xy} (MPa)	0.62	K _{xx} (W/mK)	0	G _{xy} (MPa)	0.62	K _{xx} (W/mK)	0
G _{xz} (GPa)	0.093	K _{yy} (W/mK)	0	G _{xz} (MPa)	0.267	K _{yy} (W/mK)	0
G _{yz} (GPa)	0.042	K _{zz} (W/mK)	4.52	G _{yz} (GPa)	0.118	K _{zz} (W/mK)	4.52
Poisson ratio		Specific heat		Poisson ratio		Specific heat	
v _{xy}	0.3			v _{xy}	0.3		
v _{xz}	0.001			v _{xz}	0.001		
v _{yz}	0.001			v _{yz}	0.001		

2.2.4 Sidewalls

Sidewall lamina properties are listed for a composite and for a isotropic outside fabric in Table 8 and the laminate properties are listed in Table 9. Composite lamina properties are calculated for 60% YS-90A Graphite fiber and RS-3 cyanate ester matrix materials.

Table 8: Sidewall composite lamina and fabric properties.

Structural properties		Thermal properties	
Modulus	Composite, fabric	Expansion coefficient	Composite, fabric
E11 (GPa)	526.7, 295.0	CTE1 (ppm/K)	-1.51, -0.2
E22 (GPa)	5.38	CTE2 (ppm/K)	25.98
E33 (GPa)	5.38	CTE3 (ppm/K)	25.98
Shear modulus		Heat transfer	
G12 (GPa)	3.92, 1.11	K11 (W/mK)	310, 150
G13 (GPa)	3.92	K22 (W/mK)	0.64
G23 (GPa)	2.07	K33 (W/mK)	0.64
Poisson ratio		Specific heat	
v12	0.3, 0.3		
v13	0.3		
v23	0.3		

Table 9: Sidewall laminate properties.

Structural properties		Thermal properties	
Modulus		Expansion coefficient	
E _{xx} (GPa)	242.7	CTE _{xx} (ppm/K)	-1.205
E _{yy} (GPa)	148.7	CTE _{yy} (ppm/K)	-0.692
E _{zz} (GPa)	57.2	CTE _{zz} (ppm/K)	3.189
Shear modulus		Heat transfer	
G _{xy} (GPa)	58.58	K _{xx} (W/mK)	186
G _{xz} (GPa)	2.54	K _{yy} (W/mK)	123
G _{yz} (GPa)	2.92	K _{zz} (W/mK)	0.75
Poisson ratio		Specific heat	
v _{xy}	0.422		
v _{xz}	0.312		
v _{yz}	0.245		

2.2.5 Flexures and attachments

Thin-blade flexures are to be used as the connection between the grid and the tower bottom tray closeout frame. The purpose of these flexures is to isolate the tower from grid deformations and mitigate force transfer from the grid to the towers. Flexures will be fabricated from titanium. Screws attaching the sidewalls to the trays are made of stainless steel. Properties for the screws and flexures appear in Table 10.

Table 10: Attachment fasteners and flexure properties.

	Attachments	Flexures
	Stainless steel	Titanium
Ex (GPa)	210	114
nxy	0.28	0.33
Gxy (GPa)	79	44
CTE (ppm)	1.3	8.6
Density (kg/m ³)	7700	4430
Kx (W/mK)	50	6.7

2.3 Boundary conditions

2.3.1 Tray models

Individual tray models are supported at the fastener locations in shear directions only. Because there are fasteners on all four sides along the closeouts, the models are statically stable.

2.3.2 Tower models

Support conditions for the tower models are along the bottom tray closeout bottom surface for the base-support model or along the flexure structure bottom edge for the flexure support model. In both cases the boundary supports simulate a fixed-base condition, that is all six degrees-of-freedom are restrained. It is assumed that the towers will be rigidly attached to the grid structure. It should be noted that the grid structure flexibility would contribute to the tower dynamic behavior from imposed acceleration and random vibration loads.

3. Analysis Results

Modal frequencies for both individual trays and tower structures, tower response to design condition accelerations and random vibrations are presented in this section. In some cases closed-form calculations are compared with the finite element results for verification of the FEM.

3.1 Modal analysis

3.1.1 Tray models

Calculated first mode frequencies are listed in Table 11 for the case of zero stiffness contribution from the payload layers exclusive of the detector and for the case with payload stiffness contribution. Frequencies shown in parentheses are closed-form estimates using the techniques in Appendix A. Calculated mass data is provided in Table 12. Frequencies are also listed for the face sheet modulus obtained from measured results. Theoretically the standard face

sheet laminate modulus (4 layers 0,45,90,135 degrees) should be the same as the superglast face sheet modulus (6 layers 0,60,-60,-60,60,0 degrees); however, the measured results showed a substantial difference (77GPa standard and 94GPa superglast). It is reasonable to assume that the standard face sheet unbalanced condition may be the source for the measured discrepancy.

Table 11: First mode frequency for tray models (estimates in parentheses).

Tray description	Frequency (Hz)			
	Nominal face sheet modulus		Measured face sheet modulus	
	Without payload stiffness	With payload stiffness	Without payload stiffness	With payload stiffness
Top	569	673	519 (504)	628
Standard	584	711	533 (537)	613
Superglast	462 (484)	608	450	599
Standard no-payload	718	764	656 (662)	714
Bottom	767	788	697 (688)	724

Calculated tray modal frequencies for the non-bonded corner closeouts are close (less than one percent) to the bonded tray frequencies. This is a reasonable result because the closeout walls are securely supported at the bolt locations thus effectively removing closeout deformations in the mode shape calculations. As will be shown in a subsequent section, the same cannot be said when trays are attached in a tower configuration where the non-bonded corners experience far greater local deformations in mode shapes and due to applied acceleration loads.

Table 12: Tray FEM mass distribution.

Tray component	Tray mass (Kg)				
	Base	Bottom	Superglast	Standard	Top
Closeout	0.6042	0.2725	0.2725	0.2725	0.6042
Core	0.0449	0.0571	0.1713	0.0571	0.0449
Lower face sheet	0.0339	0.0339	0.0509	0.0339	0.0339
Lower payload	0.0	0.1989	1.6941	0.4682	0.4682
Upper face sheet	0.0339	0.0339	0.0509	0.0339	0.0339
Upper payload	0.1989	0.1989	0.1989	0.1989	0.0
Total	0.9158	0.7952	2.4386	1.0645	1.1851

Frequencies as a function of mass for the 5 tray types is plotted in Figure 11 where the left curve shows the influence of the nominal face sheet composite modulus and the right curve shows the effect of the reduced measured modulus (77GPa (11.1Msi) for the base, bottom, standard, and top trays and 94GPa (13.7Msi) for the superglast tray).

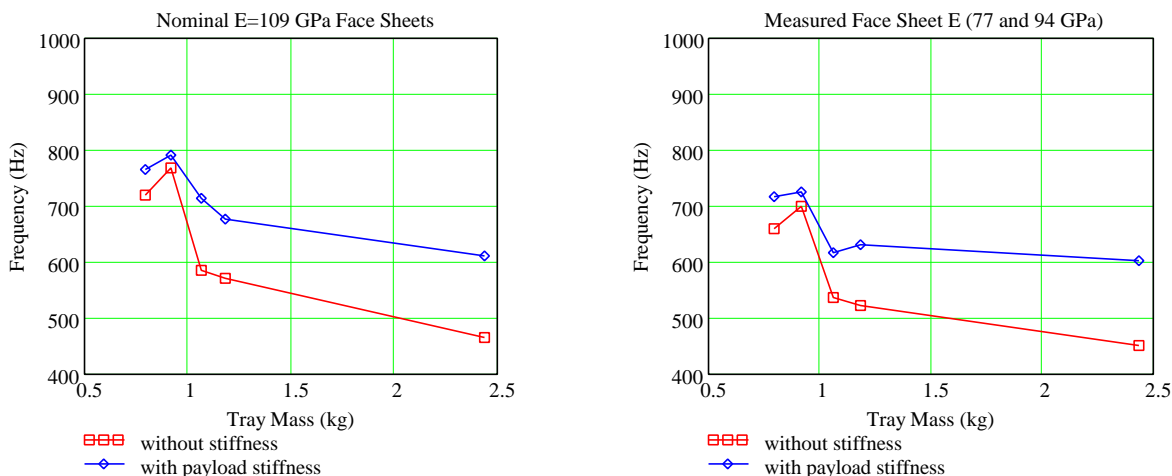


Figure 11: First mode frequency of GLAST trays as a function of mass. Plot on left is for nominal face sheet stiffness while plot on right is for measured face sheet stiffness. From left-to-right the order is standard no-payload, bottom, standard, top, and superglast.

A typical first mode shape is displayed in Figure 12.

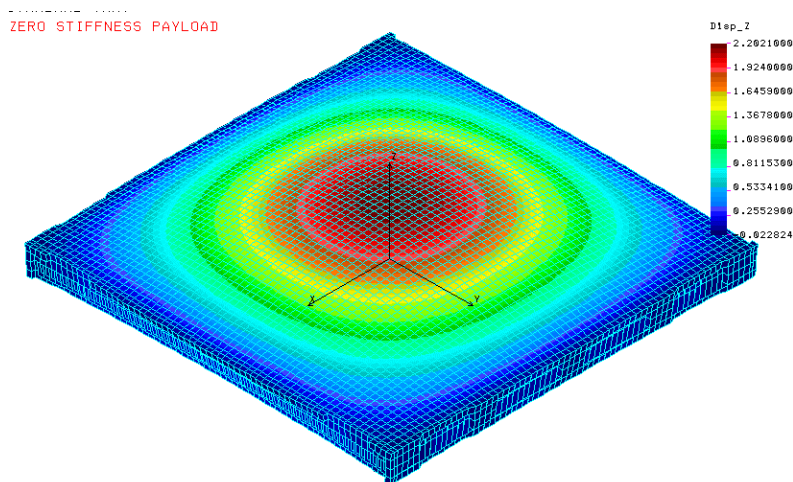


Figure 12: Typical first mode shape for FEM tray.

3.1.2 Detailed tower model

Vibration modes are calculated for three tower support configurations that simulate a corner-fixed base tray, fixed base tray, and a flexure mount design. FEM modal frequencies generated by these three configurations are listed in Table 13 and some corresponding mode shapes appear in the figures that follow. Effect of honeycomb ribbon direction is shown in Table 13 where the frequencies in parentheses denote the ribbon direction aligned normal to the detector “ladder” direction. All other frequencies are calculated for honeycomb ribbon direction parallel to the “ladder” direction. Note that there is a modest frequency shift in the tray modal

frequencies. Honeycomb ribbon direction is given by the G_{xz} shear modulus term in the honeycomb stiffness matrix.

Table 13: Detailed FEM tower modal frequencies
(frequencies in parentheses denote honeycomb ribbon direction perpendicular to detector ladder direction).

Mode	Description	Base tray fixed (Hz)	Flexure mounts (Hz)	Closeout corners removed (Hz)
1,2	Tower base bending	(363,364)	125,130 (125,130)	106,109
3	Tower plunging		294 (294)	253
4	Tower twist		375 (375)	369
5,6	Tower rocking		424,435 (424,435)	398,422
7-10	Superglast trays	(444 to 448)	447 to 485 (446 to 482)	446 to 480
11	Top tray	(527)	534 (537)	527
12-20	Standard tray	(542 to 554)	553 to 555 (546 to 549)	551 to 552

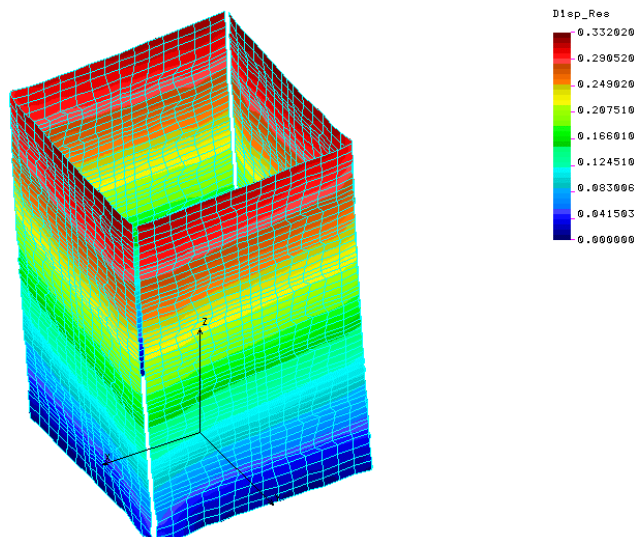


Figure 13: Mode 1 for fixed-base configuration showing sidewall deformation.

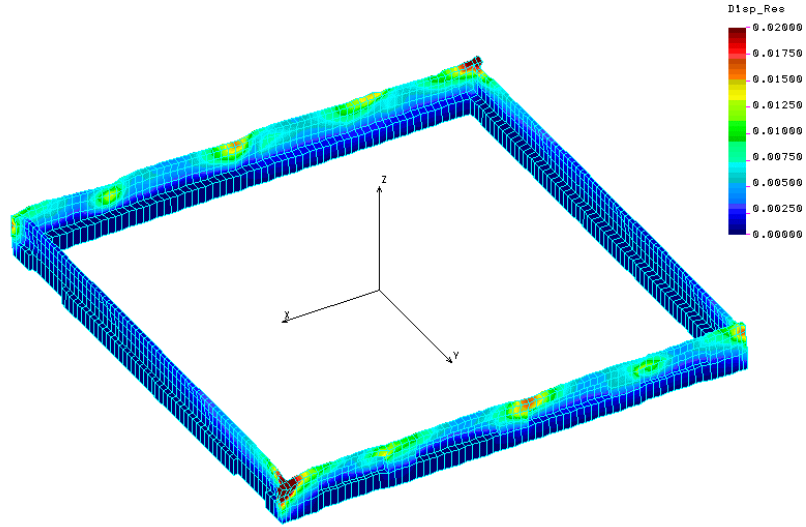


Figure 14: Mode 1 for fixed-base configuration showing bottom tray closeout deformation.

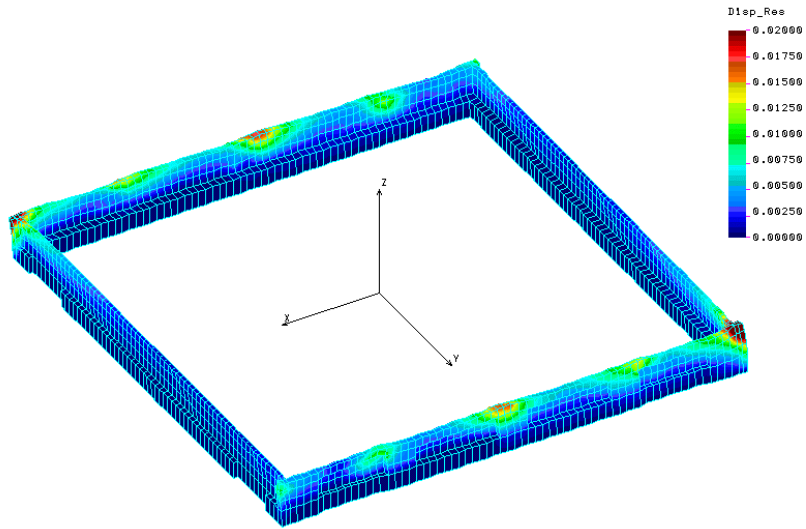


Figure 15: Mode 2 for fixed-base configuration showing bottom tray closeout deformation.

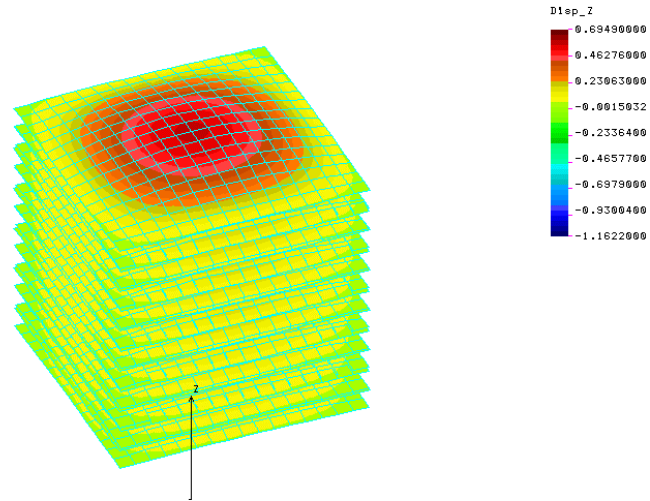


Figure 16: Mode 8 for fixed-base configuration showing standard tray deformations.

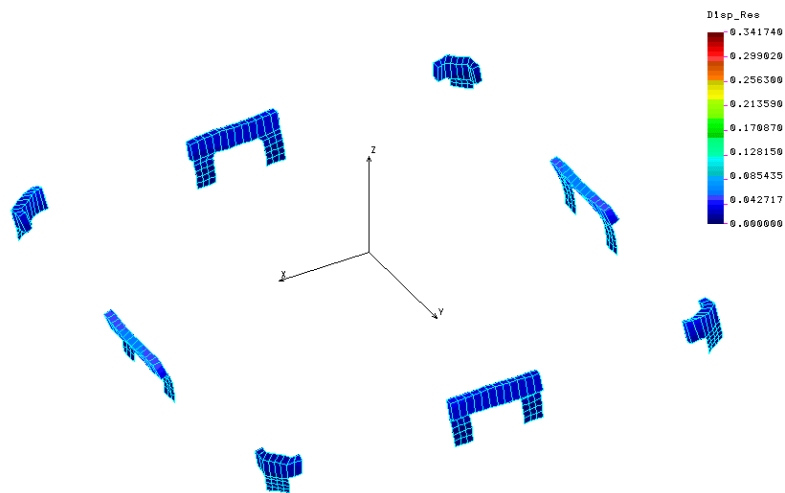


Figure 17: Mode 1 of flexure-mount configuration showing flexure deformations.

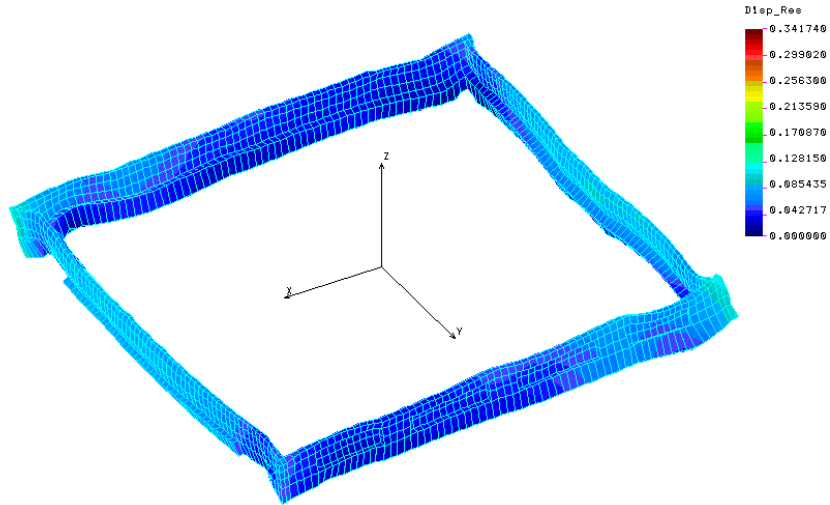


Figure 18: Mode 1 of flexure-mount configuration showing bottom tray closeout deformation.

F_Mode=1 169.945 Hz

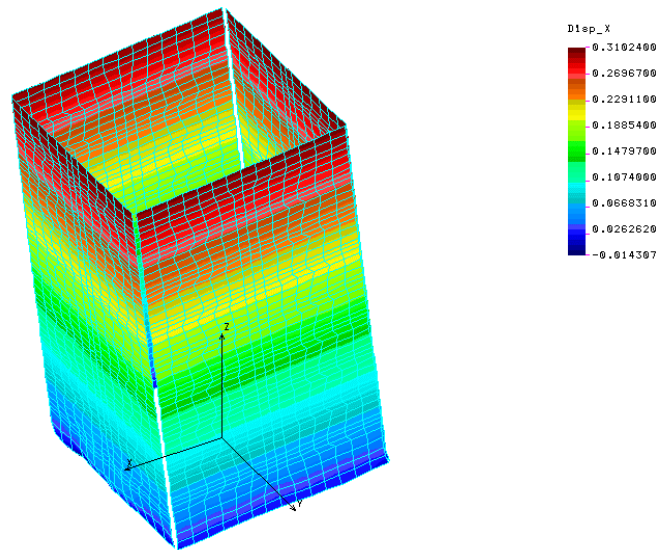


Figure 19: Mode 1 of flexure-mount configuration showing sidewall deformations (trays not shown for clarity).

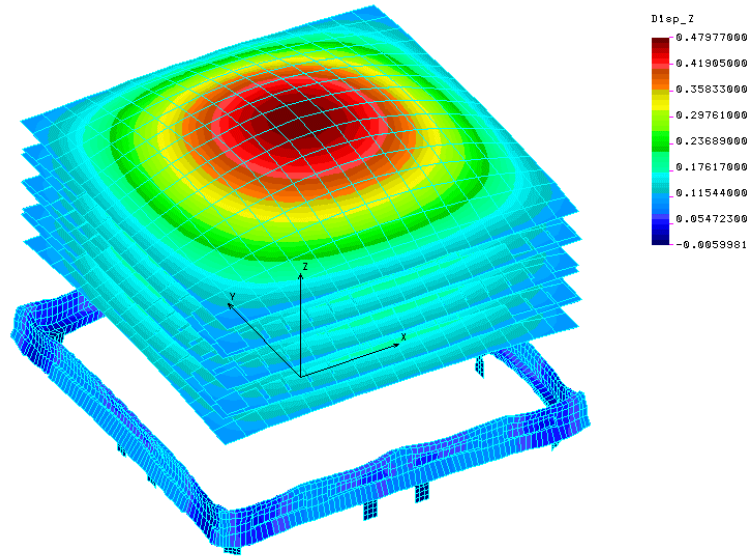


Figure 20: Mode 3 of flexure-mount configuration showing superglast tray face sheets and base closeout deformation.

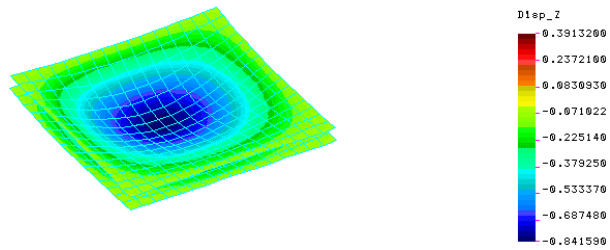


Figure 21: Mode 4 of flexure-mount configuration showing top tray face sheets.

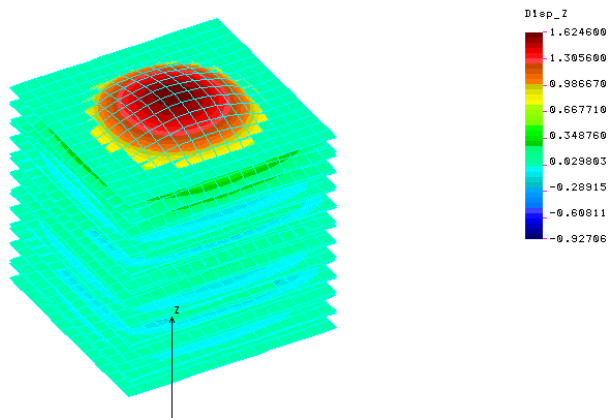


Figure 22: Mode 6 of flexure-mount configuration showing standard tray face sheets.

3.2 Random vibration analysis

3.2.1 Input spectrum

The required power spectral density (PSD) input spectrum [1] in acceleration units (G^2/Hz) and in displacement units (m^2/Hz) is shown in Figure 23.

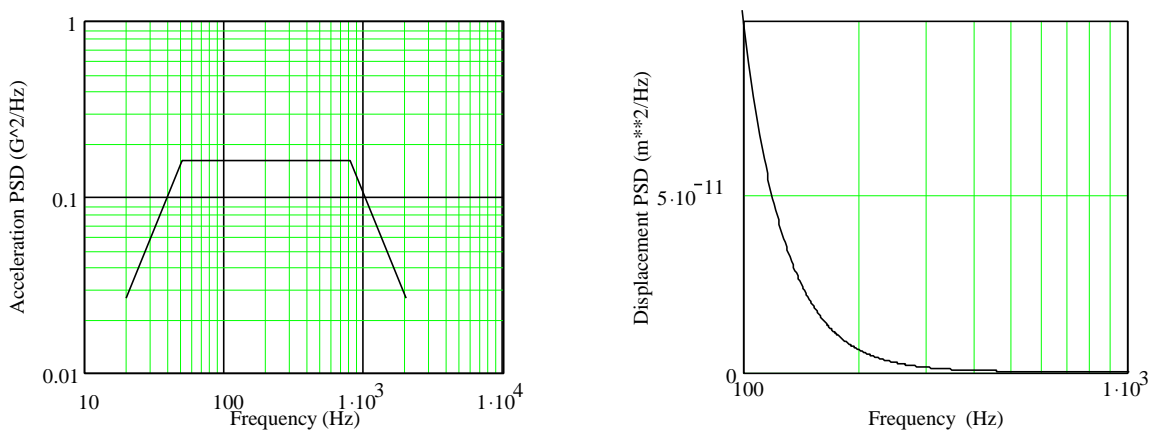


Figure 23: Support excitation input PSD acceleration and displacement spectrums.

The displacement input spectrum falls off very rapidly with frequency; therefore, higher frequency vibration modes will have diminished contribution to the tower response RMS displacement. Conversion of the acceleration spectrum into the displacement spectrum is given by

$$PSD_{msqd}(f) = \frac{g^2}{(2\pi f)^4} PSD_{Gsqd}, \quad (1)$$

where g is $9.807m/sec^2$.

3.2.2 Single tray response

A typical plot of the PSD spectrum for the midpoint on a tray with boundary support excitation to white noise appears in Figure 24. Random response at the tray midpoint is a function of frequency and damping quality factors (Q) as shown in Figure 25. These curves are produced by the methods discussed in Appendix B.

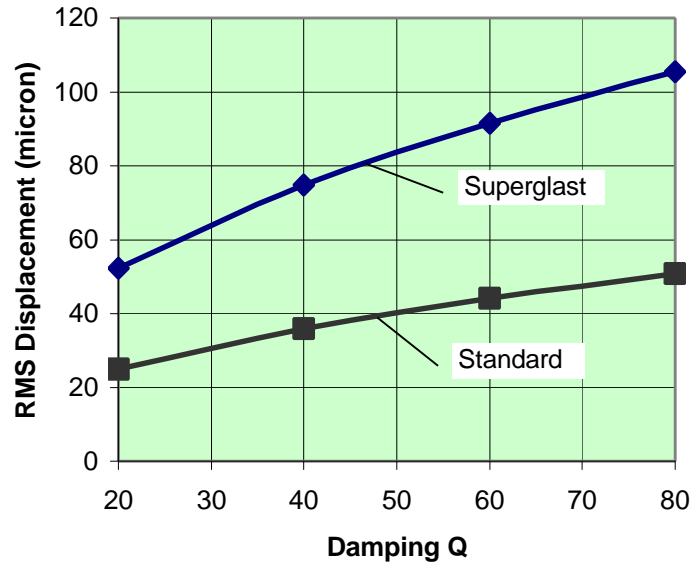


Figure 24: GLAST tray midpoint RMS response to white noise boundary excitation as a function of modal damping.

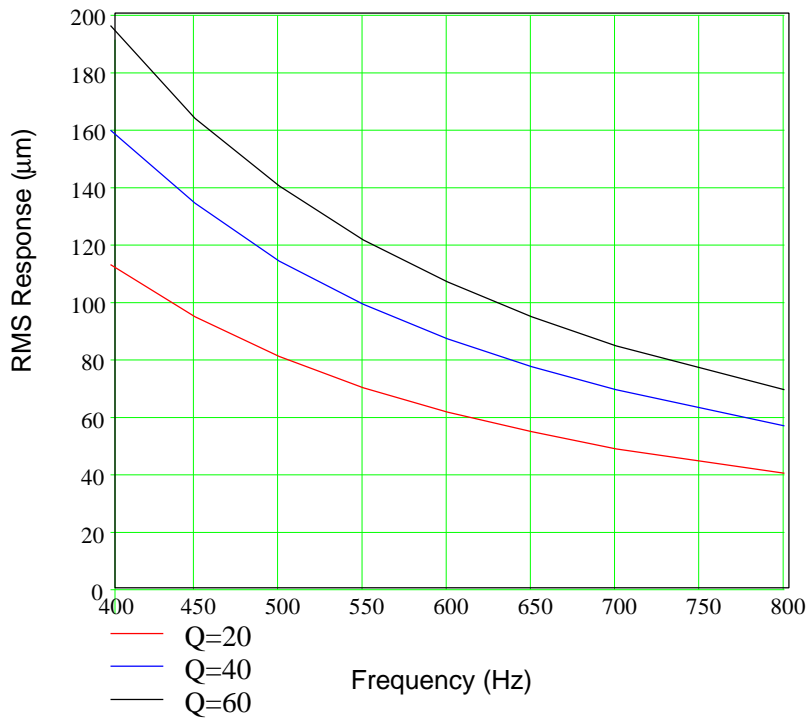


Figure 25: Closed form estimate of RMS displacement response (mm) as a function of natural frequency for vertical input PSD of $0.16g^2/Hz$.

In order to make a rough first estimate of the probability of failure, several somewhat conservative assumptions are introduced. In the present context, failure is defined as collision between neighboring trays during qualification vibration testing of the entire towers. It is

essential that the wire bonds remain intact; thus, the actual gap between trays is the distance separating potting protrusions. The simple analysis that follows conservatively assumes that neighboring trays will always deflect toward each other (as opposed to moving in phase with each other), closing the gap.

With a qualification test duration of 60 seconds^[2] and a vibration response at 700 Hz there will be 42,000 vibration cycles during the test duration. If we assume a 5% probability that any one of those peaks might exceed collision levels, then the ratio of cycles exceeding the threshold to the total number of cycles is 0.05 divided by 42,000 or 1.1905e-6.

The probability density function for the peaks of a narrow band random vibration response (single mode response to white noise) is given by a Rayleigh distribution^[5]

$$p(x) = \frac{x}{\mathbf{s}_x^2} e^{-x^2/2\mathbf{s}_x^2} \quad (6)$$

where $p(x)$ is the probability distribution, x the peak amplitude, and \mathbf{s}_x the RMS value of the narrow band process. The integral with respect to x from some specified level a to infinity is the ratio of peaks exceeding a to the total number of peaks. This integral is

$$A = \int_a^{\infty} \frac{x}{\mathbf{s}_x^2} e^{-x^2/2\mathbf{s}_x^2} dx = e^{-a^2/2\mathbf{s}_x^2} \quad (7)$$

from which the ratio a/\mathbf{s}_x is 5.2232 when $A=1.1905e-6$. This result indicates that when the half gap distance between stacked trays is 5.2 times the RMS vibration level there is a probability of 5% that one cycle may exceed this half gap displacement during the 60 second qualification test in the Z direction. The RMS values from Figure 25 are repeated in Figure 26 with the multiple 5.2 applied to the RMS amplitude to represent the required half gap displacement. The actual gap between adjacent trays is equal to twice the wire bond height plus twice the half gap distance.

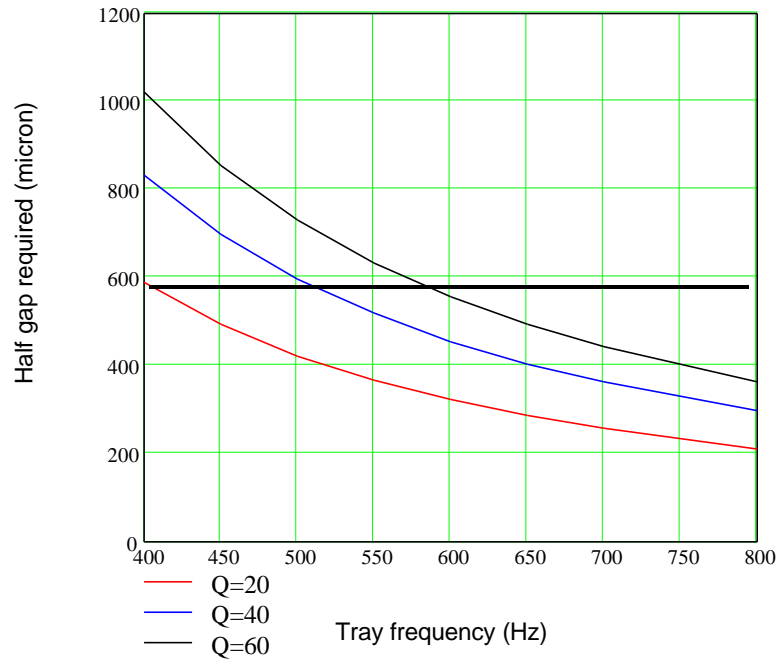


Figure 26: Estimated half gap distance required in tray stack to achieve desired probability of no contact.

3.2.3 Tower response

Tower vibration deformations resulting from the PSD input spectrum are calculated for both support configurations. Input spectrum is applied in the vertical direction at the model support points. Relative support-to-node deformations are computed. A typical response node response spectrum is shown in Figure 27.

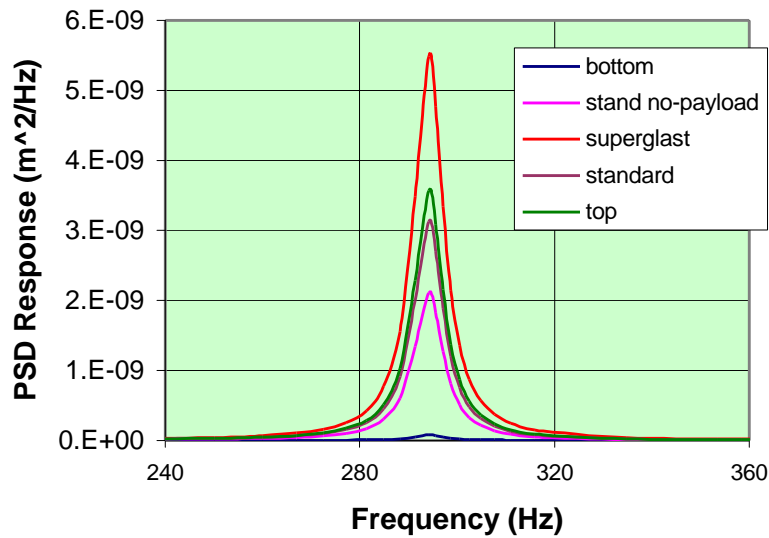


Figure 27: Tray vertical PSD response for flexure mount FEM (vertical input spectrum).

Selected tray vertical direction (Z) root mean square (RMS) response due to the input spectrum applied in the vertical direction at the support location is tabulated in Table 14. Tower response to a lateral input at the supports is listed for nodes selected along the tower top edge is given in Table 15. As described in previous section, results in parentheses denote honeycomb ribbon direction normal to the detector “ladder” direction.

Table 14: RMS tray midpoint relative displacement due to support vertical random vibration spectrum.

Tray (single tray selected among tray type)	Panel midpoint vertical (Z) RMS displacement (μm)		
	Base support	Flexure support	
	Closeout corners connected	Closeout corners connected	Closeout corners not connected
Bottom	3	30 (38)	18
Standard no-payload	84	156 (155)	200
Representative superglast	161	251 (252)	277
Representative standard	96	190 (191)	229
top	220	204 (200)	243

Table 15: RMS displacement response at selected nodes along tower top edge due to a lateral random vibration input spectrum at the supports (Q=40).

Node selected along tower top edge	RMS displacement (μm)		
	Base support	Flexure support	
	Closeout corners connected X,Y,Z dir	Closeout corners connected X,Y,Z dir	Closeout corners not connected X,Y,Z dir
midpoint along sidewall	177,17,20	761,125,181 (722,133,180)	1030,186,255
midpoint along closeout	177,17,19	761,126,190 (760,134,189)	1030,186,256
point along closeout	177,17,19	761,125,181 (760,133,180)	1030,186,271
midpoint on opposite side	159,19,2	751,128,33 (750,136,34)	1021,188,52
midpoint on other side	162,19,3	753,128,35 (752,135,37)	1022,188,54
Maximum (any point)	178,19,30	761,128,210 (760,136,210)	1030,189,315

3.3 Static analysis

3.3.1 Static acceleration loads

Static acceleration loads defined as 1) liftoff and transonic (LAT) and 2) main engine cutoff (MECO) are individually applied to the FEM boundary supports. These acceleration loads are listed in Table 16. Maximum displacements, stresses, and connecting bolt loads are presented in Table 17 for the base support condition Table 18 for the flexure support condition and Table 19 for the flexure support and closeout corners not connected. As before, results in parentheses refer to honeycomb core ribbon aligned perpendicular to the detector ladder direction.

Table 16: Defined acceleration loads.

	Liftoff and transonic (LAT)		Main engine cutoff (MECO)	
	Vertical	Lateral	Vertical	Lateral
Acceleration (G)	3.25	4.0	6.6	0.1
Acceleration (m/s ²)	31.88	39.24	64.75	0.98

Table 17: Deformations, forces, stresses due to static acceleration loads for base support FEM.

Displacement, stress, or load description	Liftoff and transonic		Main engine cutoff	
	SI units	Engineering units	SI units	Engineering units
Structure:				
Maximum displacement	12 μm	0.46 mil	14 μm	0.55 mil
Maximum VM nodal stress	16.40 MPa	2.38 ksi	4.82 MPa	0.70 ksi
Maximum VM element stress	8.28 MPa	1.20 ksi	2.38 MPa	0.35 ksi
Attachment bolt:				
Maximum axial force	3.11 N	0.70 lbf	2.80 N	0.63 lbf
Maximum axial stress	0.64 MPa	0.09 ksi	0.57 MPa	0.08 ksi
Maximum shear VT	147.0 N	33.05 lbf	79.8 N	17.94 lbf
Maximum shear VS	80.6 N	18.12 lbf	24.0 N	5.40 lbf
Maximum stress	56.6 MPa	8.21 ksi	26.9 MPa	3.90 ksi

Table 18: Deformations, forces, stresses due to static acceleration loads for the flexure supported FEM.

Displacement, stress, or load description	Liftoff and transonic		Main engine cutoff	
	SI units	Engineering units	SI units	Engineering units
Structure:				
Maximum displacement	87(87) μm	3.43 mil	28(27) μm	1.10 mil
Maximum VM nodal stress	98.5(98.3) MPa	14.3 ksi	50.0(50.0) MPa	7.3 ksi
Maximum VM element stress	133.4(132.7) MPa	19.3 ksi	67.6(67.0) MPa	9.8 ksi
Attachment bolt:				
Maximum axial force	11.80(11.95) N	2.65 lbf	10.34(10.44) N	2.33 lbf
Maximum axial stress	2.40(2.44) MPa	0.35 ksi	2.11(2.13) MPa	0.31 ksi
Maximum shear VT	181.5(181.0) N	40.8 lbf	104.5(104.3) N	23.5 lbf
Maximum shear VS	146.5(147.2) N	32.9 lbf	74.2 (74.3) N	16.7 lbf
Maximum stress	133.4(132.7) MPa	19.3 ksi	67.6(67.0) MPa	9.8 ksi

Table 19: Deformations, forces, stresses, due to static acceleration loads for the flexure supported FEM and closeout corners not connected.

Displacement, stress, or load description	Liftoff and transonic		Main engine cutoff	
	SI units	Engineering units	SI units	Engineering units
Structure:				
Maximum displacement	132 μm	5.20 mil	34 μm	1.34 mil
Maximum VM nodal stress	114.3 MPa	16.6 ksi	36.5 MPa	5.3 ksi
Maximum VM element stress	197.4 MPa	28.6 ksi	111.6 MPa	16.2 ksi
Attachment bolt:				
Maximum axial force	12.52 N	2.82 lbf	15.51 N	3.49 lbf
Maximum axial stress	2.55 MPa	0.37 ksi	3.16 MPa	0.46 ksi
Maximum shear VT	181.0 N	40.7 lbf	137.1 N	30.8 lbf
Maximum shear VS	137.0 N	30.8 lbf	58.4 N	13.1 lbf
Maximum stress	197.4 M Pa	28.6 ksi	111.6 MPa	16.2 ksi

The figures that follow show the calculated FEM results for the static load cases.

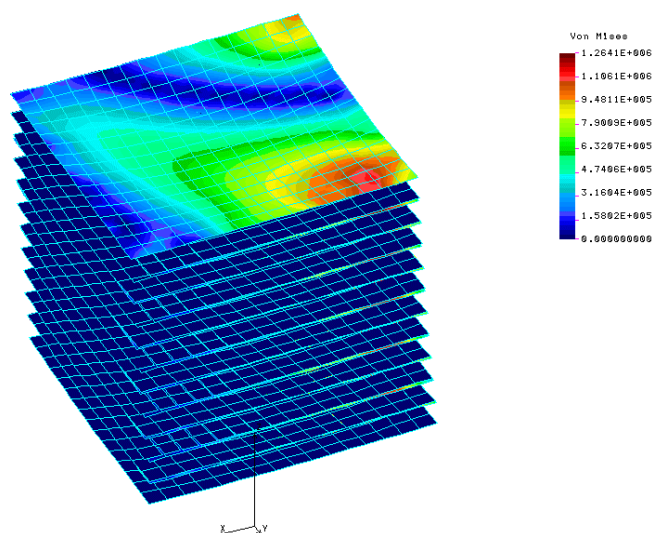


Figure 28: Stress distribution in standard tray face sheets for fixed-base FEM – load case 1.

NUJE STRESS

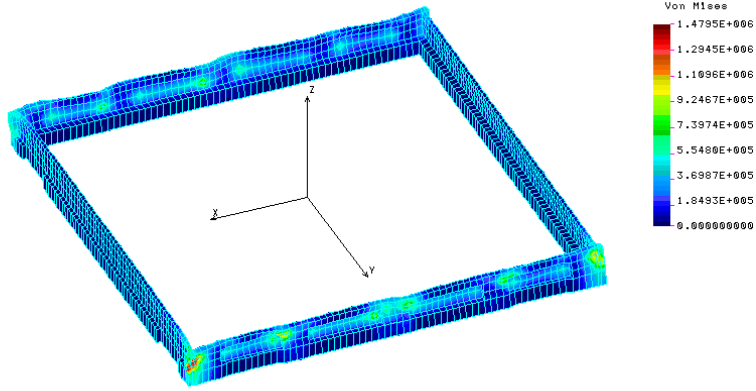


Figure 29: Stress distribution in base tray closeout for fixed-base FEM – load case 1.

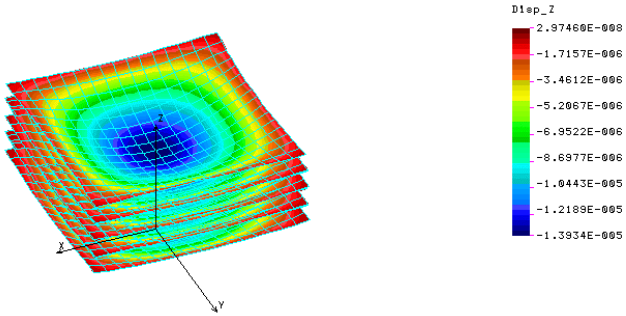


Figure 30: Vertical displacement distribution in superglast tray face sheets for fixed-base FEM – load case 2.

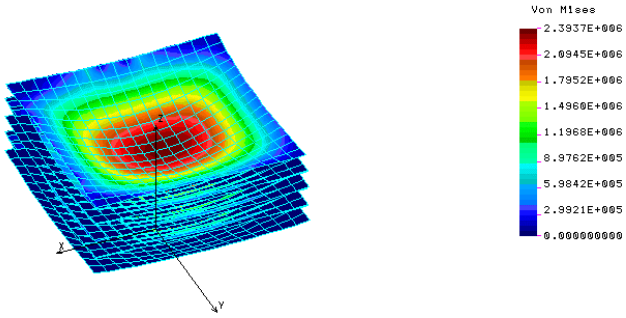


Figure 31: Von Mises stress distribution in superglast face sheets for fixed-base FEM – load case 2.

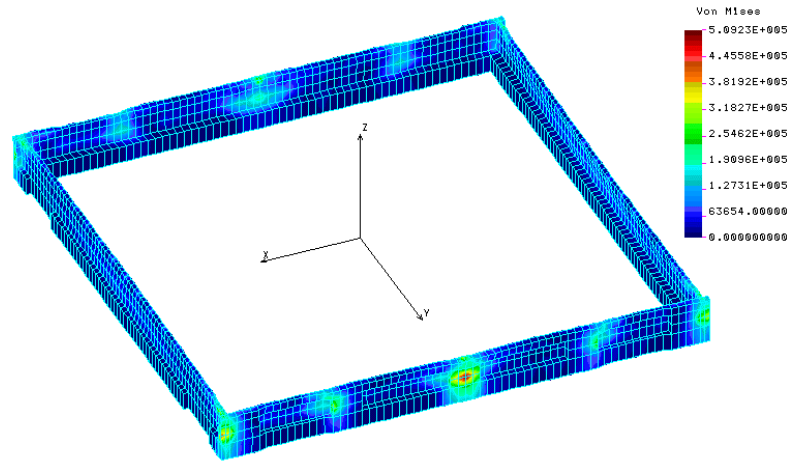


Figure 32: Von Mises stress distribution in base tray closeout for fixed-base FEM – load case 2.

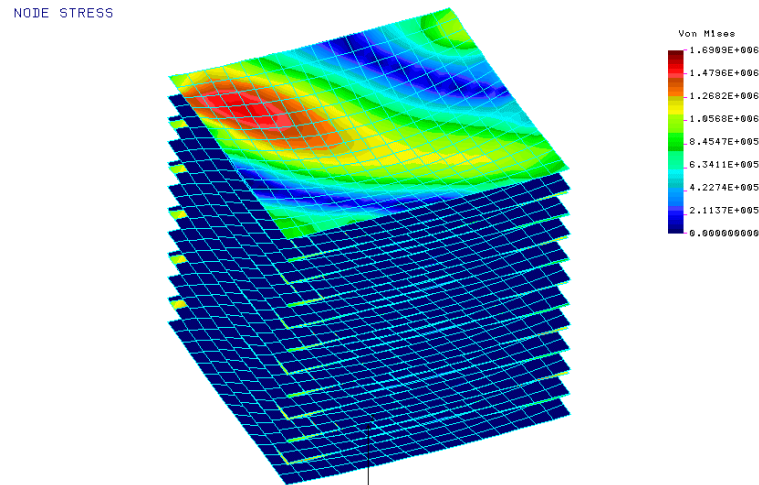


Figure 33: Von Mises nodal stress distribution in standard tray face sheets for fixed-base FEM – load case 2.

ELEMENT STRESS

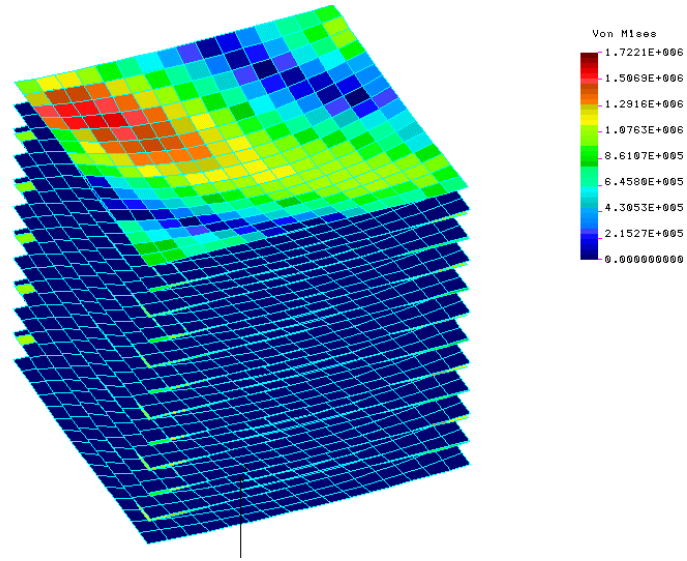


Figure 34: Von Mises element stress distribution in standard tray face sheets for fixed-base – load case 2.

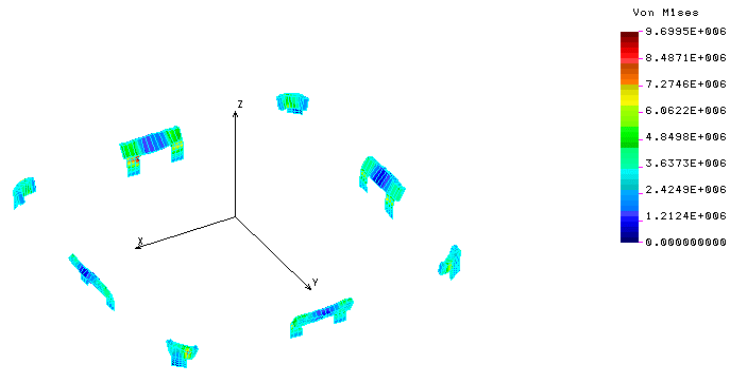


Figure 35: Von Mises nodal stress distribution in flexures for flexure-mount – load case 1.

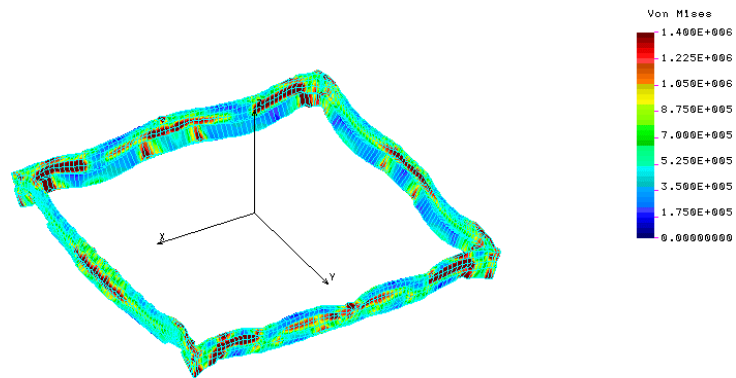


Figure 36: Von Mises nodal stress distribution in base tray closeout for flexure-mount – load case 1.

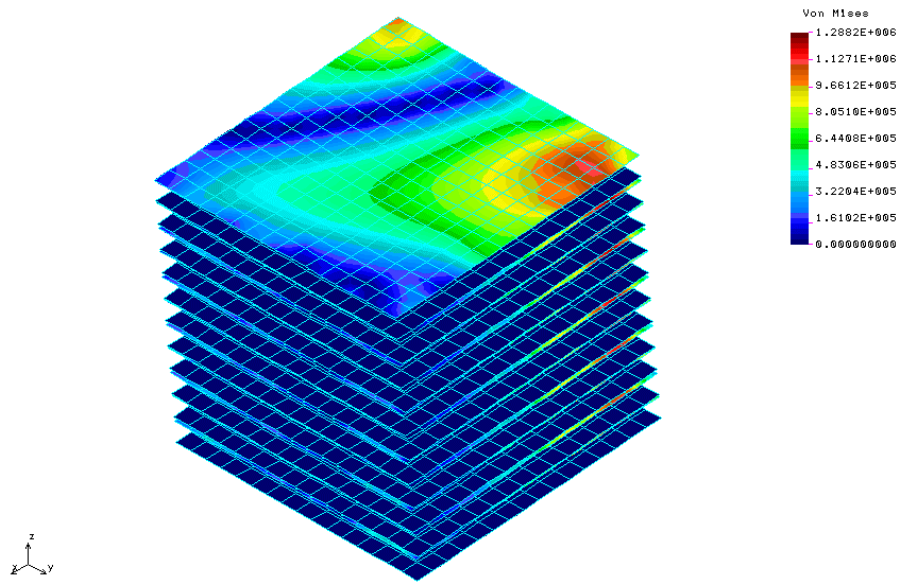


Figure 37: Von Mises nodal stress distribution in standard tray face sheets for flexure-mount – load case 1.

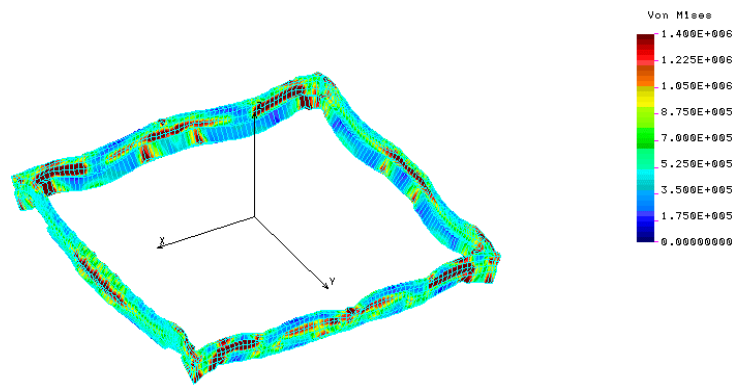


Figure 38: Von Mises nodal stress distribution in base tray closeout for flexure-mount – load case 2.

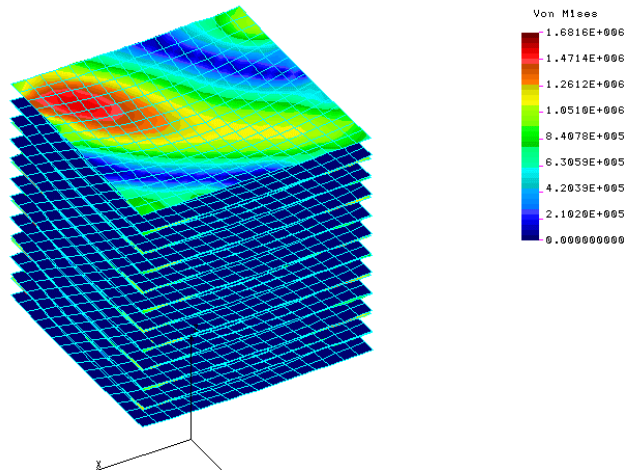


Figure 39: Von Mises nodal stress distribution in standard tray face sheets for flexure-mount – load case 2.

3.3.2 Bottom tray corner closeout loads (flexure mount configuration)

Shear stresses generated by the static acceleration loads are shown in the figures that follow. From these stresses an approximate base tray corner closeout load may be calculated.

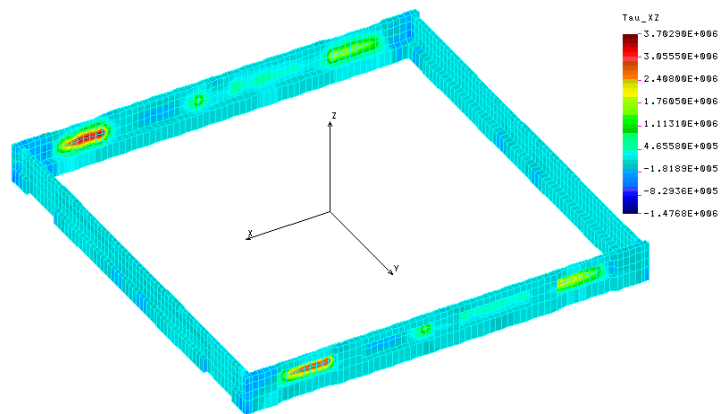


Figure 40: Shear stresses in the XZ plane in the bottom tray closeout for the flexure support configuration and load case 1.

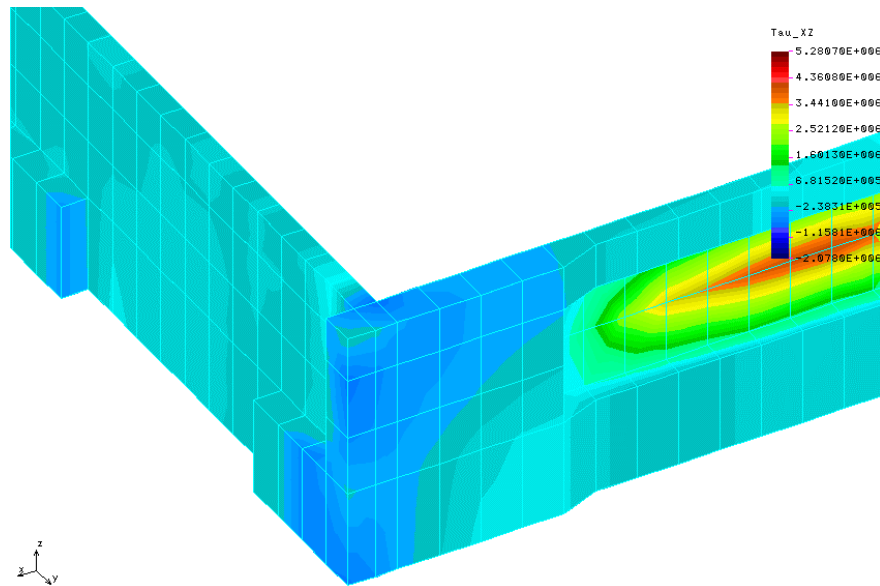


Figure 41: Nodal shear stresses in the XZ plane in the bottom tray closeout for the flexure support configuration and load case 1.

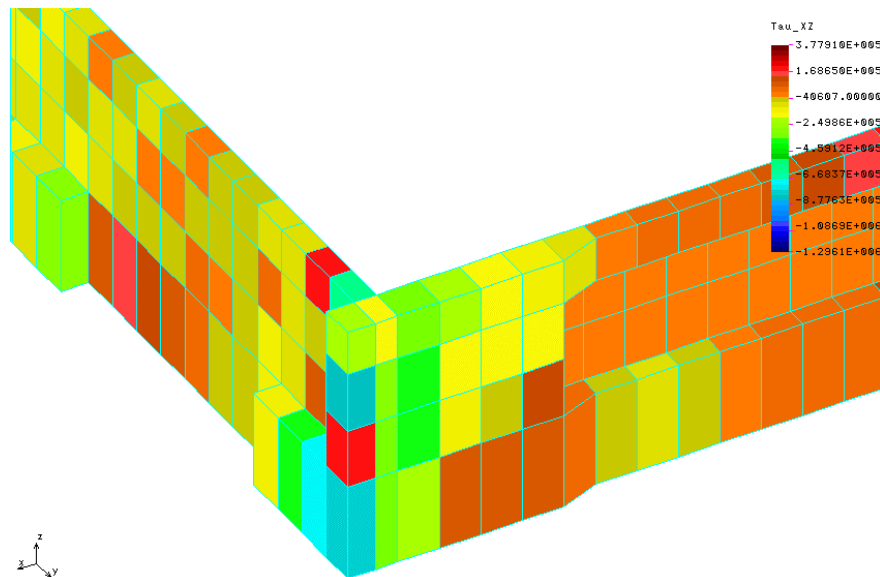


Figure 42: Element shear stresses in the XZ plane in the bottom tray closeout for the flexure support configuration and load case 1.

Nodal average shear stress in the XZ plane in a base closeout corner is about 0.40MPa for load case 1 as shown in Figure 41. The element stress is about 0.40MPa as shown in Figure 42. Corner forces and the subsequent peel face sheet stress (for a non-bonded corner) can be estimated by the product of area and shear stress. The width and height of the closeout section is 5mm and 35mm respectively; thus the force is approximately 70N (16 lbf).

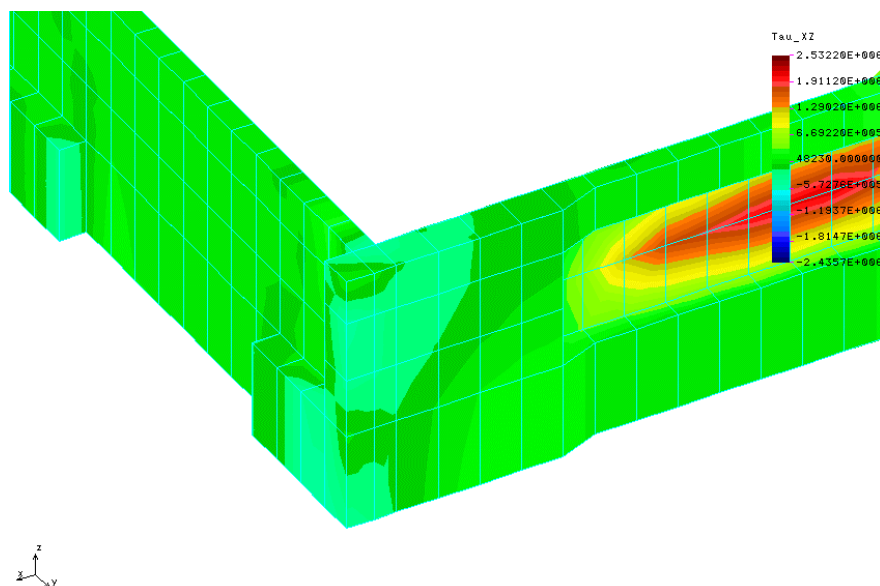


Figure 43: Nodal shear stresses in the XZ plane in the bottom tray closeout for the flexure support configuration and load case 2.

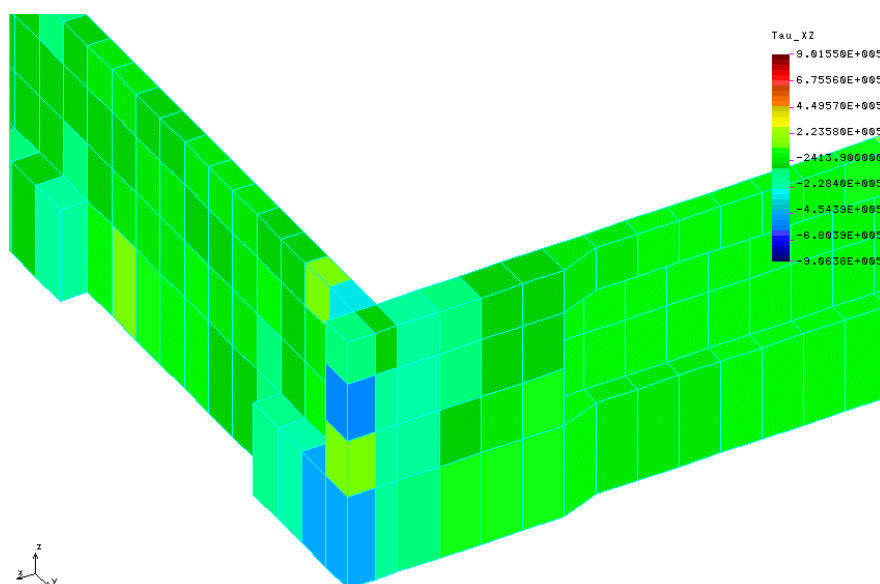


Figure 44: Element shear stresses in the XZ plane in the bottom tray closeout for the flexure support configuration and load case 2.

Nodal average shear stress in the XZ plane in a base closeout corner is about 0.23MPa for load case 2 as shown in Figure 43. The element stress is about 0.25MPa as shown in Figure 44. These stresses are lower than those associated with load case 1 even though the vertical acceleration is considerably larger (6.6G versus 3.25G); however, there is a much larger lateral acceleration for case 1 (4.0G versus 0.1G) that will contribute to the bending moment at the support location.

3.3.3 Assembly distortion

Two assembly load conditions are examined. The first assumes that all sidewalls are intact and the second assumes that one sidewall is missing. A load of 20N is applied at diagonal corners as shown in Figure 45 where all sidewalls are in place. Displacements resulting from the same applied assembly load is shown in Figure 46 for the case of a missing sidewall. A summary of the corner displacements is given in Table 20.

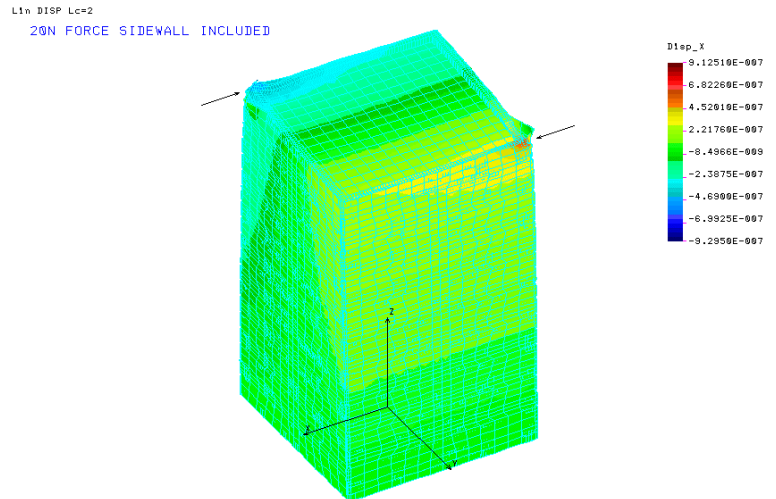


Figure 45: Static assembly loads applied to fixed-base model showing displacements along applied force direction (all sidewalls in place).

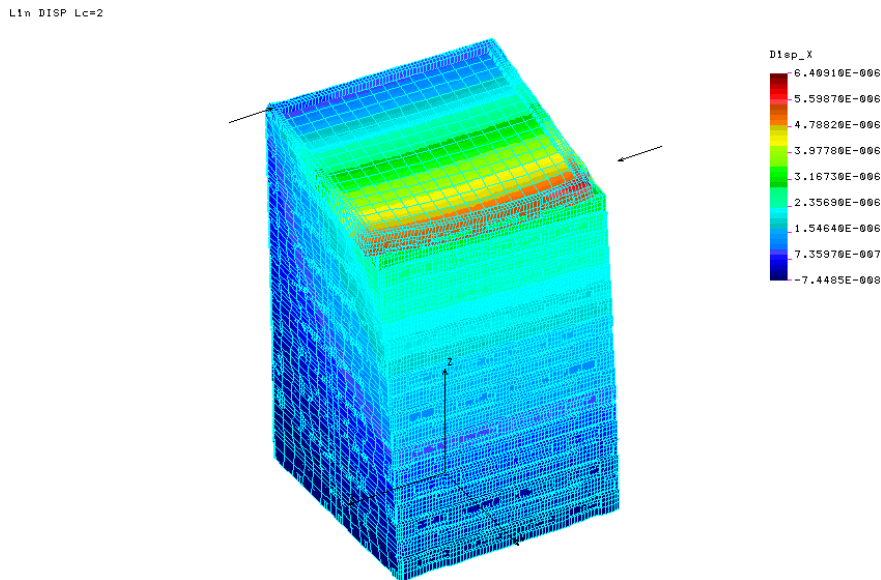


Figure 46: Static assembly loads applied to fixed-base model showing displacements along applied force direction (near sidewall missing).

Table 20: Calculated corner node displacement during assembly for fixed-base FEM.

Configuration	Corner node	Displacements (μm)		
		UX	UY	UZ
All sidewalls intact	62184	0.912	0.064	0.247
	62972	-0.929	-0.068	0.256
One missing sidewall	62184	6.409	1.410	-0.420
	62972	0.107	-1.218	-0.102

3.3.4 Grid deformation induced stress

Support flexure bending stress due to grid thermal expansion deformations is shown in Figure 47. If it is assumed that the flexure blade is fixed (no rotation), the bending stress is given by

$$s = \frac{6 E c \Delta}{L^2} \quad (10)$$

where E , c , L , and Δ are the modulus of elasticity (Titanium=16E6 psi), blade half width (0.38mm), blade length (18mm), and the prescribed grid thermal deformation. A deformation of 0.5mm (0.25mm thermal growth plus 0.25mm machine tolerance) on each side of the grid generates a stress of about 0.39GPa (56ksi) that is well below the elastic limit of 1.10GPa (159ksi) and ultimate strength of 1.17GPa (169ksi) for 6AL4V titanium alloy.

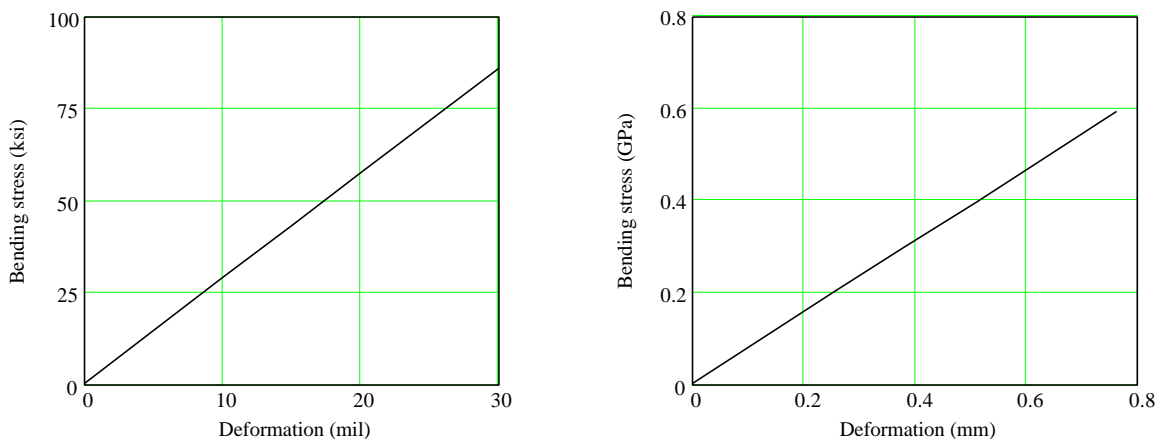


Figure 47: Flexure bending stress induced by grid thermal deformation.

Attachment bolt loads can be estimated by assuming the flexure bending moment is resisted by the bolt-cap couple and the resulting bolt stress is

$$M = \frac{6 E I \Delta}{L^2} \quad (11)$$

$$s_b = \frac{M}{f R_b A_b} \quad (12)$$

where I , f , R , and A (subscript b denotes bolt) are the flexure area moment-of-inertia, bolt couple factor (approximately 1.1), radius, and area; respectively. Figure 48 displays the bolt stress as a function of grid thermal deformation.

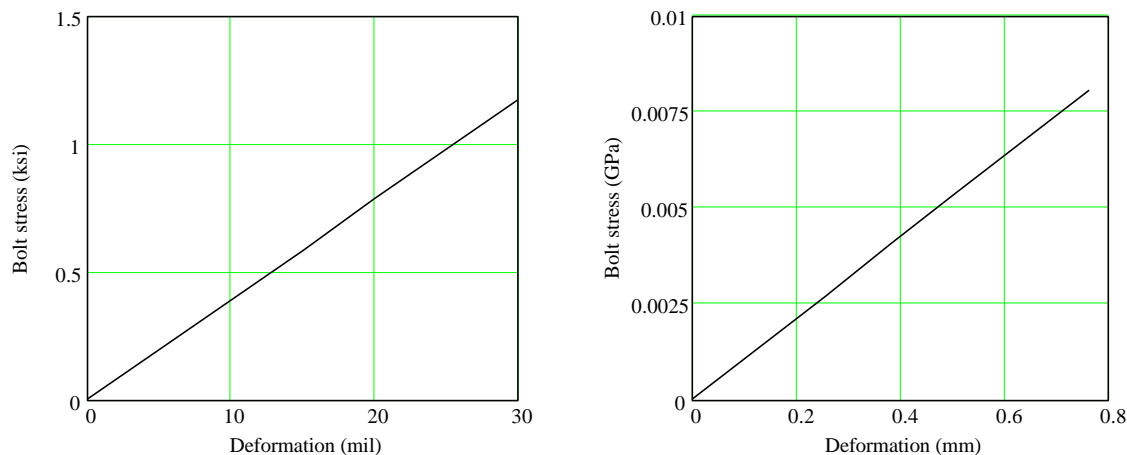


Figure 48: Flexure support bolt stress as a function of grid thermal deformation.

3.4 Thermal analysis

Electronic devices generate about ½ (updates are described in section 4.4) watt heat power on two sides of each closeout frame. This heat power must flow from each closeout through the connection with the sidewalls, down the sidewalls, into the bottom closeout frame and into the grid structure. With a direct thermal connection from the base tray to the grid, the temperature gradient from the bottom tray to the top tray is about 16.5 deg C.

Calculated orthotropic conductivities for the laminate sidewalls are 186W/mK along the vertical direction and 123W/mK in the horizontal direction (see Table 9). Measured conductivities are 255W/mK and 122W/mK in the vertical and horizontal directions, respectively. These measured conductivities are possible if the fiber conductivity is greater than the reported value and if there are more fibers in the vertical direction. For example, if the fiber conductivity is 650W/mK rather than the published 500W/mK and if one of the lamina directions is 22.5 deg rather than the expected 45 deg, then the calculated laminate conductivities are 255W/mK and 133W/mK matching the test results rather well. The fiber axial conductivity dominates the composite lamina conductivity and the resulting laminate conductivity.

Closed-form analysis indicates about 0.99 deg C trough the attachments securing the sidewalls to the bottom closeout and 14.2 deg C along the sidewalls to the top closeout. There is approximately 0.5 to 0.8 degree rise in the tray from the bolts to the middle of the heat generation source.

Finite element results appear in the following figures where it is assumed that the bottom closeout frame base is held at zero degrees. Temperature change through the bolts is about 0.03 degree C based on the assumed effective contact resistance (represented by bolts 0.5mm in length) between the closeout frame and the sidewall. This effective contact resistance can be

adjusted to simulate future measured data or models that account for contacting surface roughness and bolt loads.

Figure 49 shows the sidewall temperature profile, Figure 50 and Figure 51 show the temperature distribution in the top tray and base tray closeout frames, respectively.

THERMAL Step=1

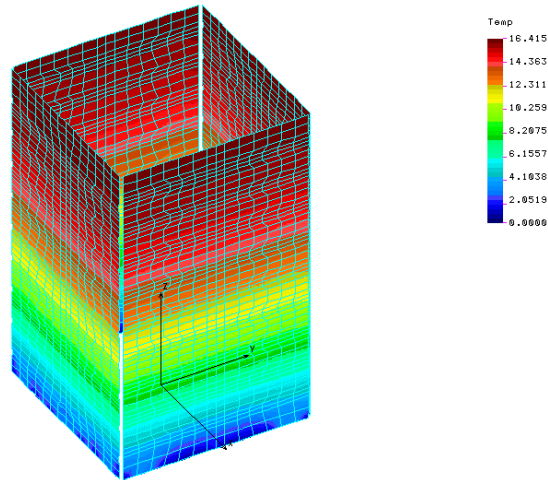


Figure 49: Sidewall temperature distribution for one watt thermal power per tray.

THERMAL Step=1

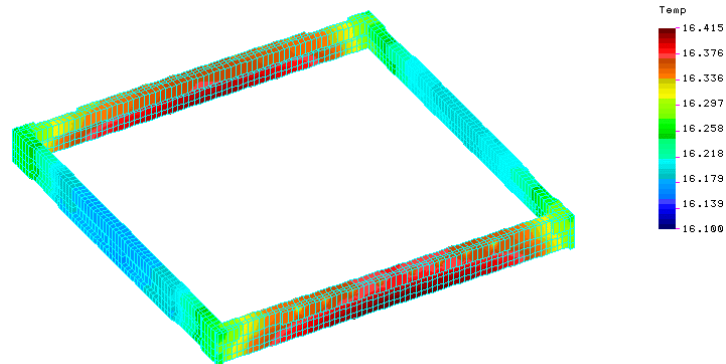


Figure 50: Temperature distribution in top tray closeout generated by a one-watt thermal power input.

THERMAL Step=1

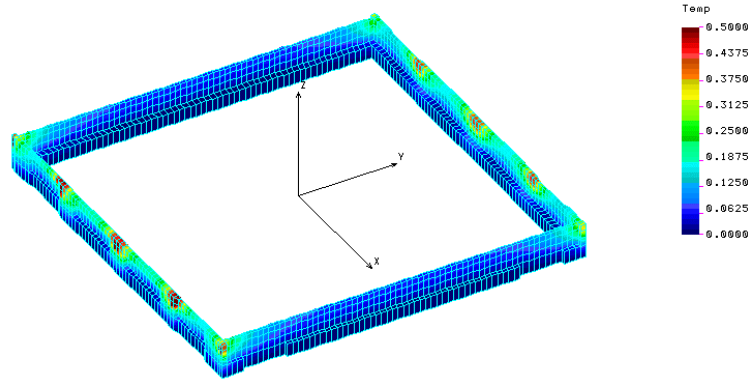


Figure 51: Temperature distribution in base tray closeout generated by a one-watt heat power input for each of nineteen trays.

4. Conductive Elastomer and Closeout Frame Redesign

It is proposed that a highly thermally conductive elastomer be added to the bottom closeout bottom surface. The purpose of this elastomer is to reduce the overall sidewall temperature gradient as described in the previous section. The ring will increase rigid body frequencies and thus reduce the tracker vibration response to the random vibration input spectrum. Increased closeout wall thickness generates changes in resonant frequencies. This section summarizes the calculated results obtained incorporating these design changes.

4.1 Tracker frequencies

The highly thermally conductive elastomer added between the tracker tower and the grid brings changes to the tracker rigid body frequencies as well as substantially reducing the tracker sidewall temperatures. Frequency comparisons for various configurations are shown in Table 21. The baseline design denotes a configuration where the honeycomb ribbon direction is perpendicular to the ladder direction (or parallel to the MCM closeout wall), tray facesheet properties are adjusted for measured properties, and the tracker tower is mounted on the design flexures. These baseline design frequencies are the same as the flexure mount frequencies given in Table 13.

Closeout MCM wall thickness is increased from 3 to 5mm in the revised closeout design. As can be seen in Table 21, the increased wall stiffness tends to increase tower rigid body frequencies as might be expected. These rigid body frequencies are a function of the tracker inertia properties and the stiffness contribution of the flexures and base tray.

Table 21: Calculated frequencies for baseline design, revised closeout design, and revised closeout plus elastomer.

Mode	Description	Baseline design (Hz)	Revised closeout (Hz)	Base elastomer added (Hz)
1,2	Tower base bending	125,130	132,137	162,174
3	Tower plunging	294	315	
4	Tower twist	375	358	
5,6	Tower rocking	424,435	426,437	365
7-10	Superglast trays	446 to 482	451 to 488	450 to 494
11	Top tray	537	536	537
12-20	Standard trays	546 to 549	557 to 559	557 to 559

4.2 Random response

Calculated random responses are presented in Table 22 and Table 23 for vertical and horizontal excitation, respectively. As in the previous section, results are given for the baseline, revised closeout, and revised closeout plus base elastomer designs.

Table 22: RMS tray midpoint relative displacement due to vertical random vibration spectrum (Q=40).

Tray (single tray selected among tray type)	Panel midpoint vertical (Z) RMS displacement (? m)		
	Baseline design	Revised closeout	Elastomer added
Base	38	124	20
Representative bottom	155	136	91
Representative superglast	252	244	236
Representative standard	191	174	137
top	200	191	165

Table 23: RMS displacement response at selected nodes along the tower top edge due to a lateral random vibration input spectrum at the supports (Q=40).

Node selected along tower top edge	RMS displacement (µm)		
	Baseline design X,Y,Z dir	Revised closeout X,Y,Z dir	Elastomer added X,Y,Z dir
midpoint along sidewall	722,133,180	697,129,154	494,21,123
midpoint along closeout	760,134,189	697,130,162	494,23,125
point along closeout	760,166,180	697,129,154	494,21,123
midpoint on opposite side	750,136,34	687,132,30	484,22,5
midpoint on other side	752,135,37	690,132,32	486,22,10
Maximum (any point)	760,136,210	697,133,182	495,44,134

4.3 Static loads

Static forces and stresses due to steady-state acceleration loads are presented in Table 24 for the revised closeout design with flexure support. Comparison between the present results and the baseline results (Table 18) shows a modest decrease in displacements and a slight increase in

attachment bolt loads. These trends are reasonable when noting that there is a modest change in the rigid body frequencies as shown by the comparisons listed in Table 21. While there is a small increase in mass due to the thicker closeout walls, the stiffness effect is slightly greater resulting in slightly greater frequencies. It is reasonable that the displacements would decrease (stiffer structure) and the loads increase as the mass increases for the same acceleration levels.

Table 24: Deformations, forces, stresses due to static acceleration loads for the revised closeout with flexure support.

Displacement, stress, or load description	Liftoff and transonic		Main engine cutoff	
	SI units	Engineering units	SI units	Engineering units
Structure:				
Maximum displacement	78 μm	3.07 mil	25 μm	0.98 mil
Maximum VM nodal stress	101.0 MPa	14.65 ksi	43.1 MPa	6.25 ksi
Maximum VM element stress	106.0 MPa	15.37 ksi	75.6 MPa	10.96 ksi
Attachment bolt:				
Maximum axial force	14.4 N	3.24 lbf	11.6 N	2.61 lbf
Maximum axial stress	2.9 MPa	0.42 ksi	2.36 MPa	0.34 ksi
Maximum shear VT	185.8 N	41.77 lbf	105.1 N	23.62 lbf
Maximum shear VS	161.9 N	36.40 lbf	79.6 N	17.89 lbf
Maximum stress	106.0 MPa	15.37 ksi	75.6 MPa	10.96 ksi

As might be expected, further reductions in displacements, stresses, and bolt loads are generated by the additional elastomer support system as evidenced in Table 25. In this case the frequency increase is more pronounced because there is a substantial stiffness increase accompanied by a negligible mass increase.

Table 25: Deformations, forces, stresses due to static acceleration loads for the revised closeout with flexure and elastomer support.

Displacement, stress, or load description	Liftoff and transonic		Main engine cutoff	
	SI units	Engineering units	SI units	Engineering units
Structure:				
Maximum displacement	49 μm	1.93 mil	20 μm	0.79 mil
Maximum VM nodal stress	55.3 MPa	8.02 ksi	30.6 MPa	4.44 ksi
Maximum VM element stress	69.1 MPa	10.02 ksi	59.2 MPa	8.59 ksi
Attachment bolt:				
Maximum axial force	7.82 N	1.76 lbf	11.70 N	2.36 lbf
Maximum axial stress	1.59 MPa	0.23 ksi	2.81 MPa	0.41 ksi
Maximum shear VT	133.7 N	30.06 lbf	121.2 N	27.25 lbf
Maximum shear VS	88.0 N	19.78 lbf	46.0 N	10.34 lbf
Maximum stress	69.1 MPa	10.02 ksi	59.2 MPa	8.59 ksi

4.4 Thermal analysis

Thermal load per TCMC is updated from 0.5 Watt to 0.35 Watt for the present analysis. With the addition of the elastomer the heat load is very efficiently transferred from the sidewalls into the base tray and through the elastomer to the grid. The elastomer bottom surface is fixed at zero degree C implying that the grid is an infinite heat sink at zero degree. Figure 52 shows the sidewall temperature contours. The maximum temperature drop is 11.8 degree C.

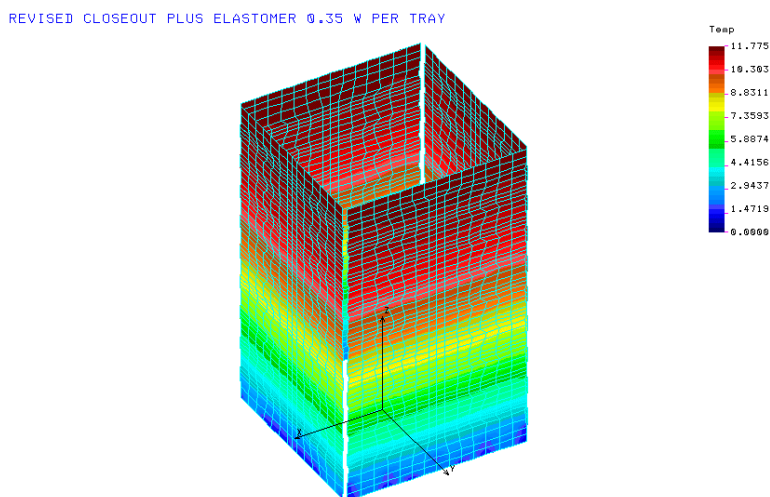


Figure 52: Sidewall temperature using elastomer base.

5. Summary and Conclusions

This technical note presents the results for static, dynamic, and thermal finite element model analysis of the GLAST tracker tower. Loads, deformations, and temperatures are within acceptable limits provided the tracker tower is supported by flexures and an elastomer material between the bottom tray and the grid.

6. References

1. COSMOS/M 2.0 for Windows Platforms, Structural Research and Analysis Corporation, Los Angeles, CA.
2. "GLAST Design Material Properties for Finite Element Models", HYTEC Inc., HTN-102050-0013-E.
3. "GLAST Tray Structural and Thermal Deformations", HYTEC Inc., HTN-102060-0006.
4. "General Environmental Verification Specification for STS & ELV Payloads, Subsystems, and Components", System Reliability and Safety Office, NASA/GODDARD SPACE FLIGHT CENTER, GEVES-SE REV A, June 1996.
5. Crandall and Mark, Random Vibration in Mechanical Systems, Academic Press, New York, 1963.
6. AEROWEB - Honeycomb Sandwich Design Technology, August 1955.
7. Warren C. Young, Roark's Formulas for Stress and Strain, McGraw-Hill Inc., Sixth Edition, 1989.
8. Hurty and Rubinstein, Dynamics of Structures, Prentice Hall, Englewood Cliffs, NJ, 1964.

Appendix A: Closed-Form Modal Frequency Calculations

Calculated Et products are combined with the core properties (Ez , Gxz , Gyz) to estimate the tray midpoint deformation due to an applied uniform surface pressure. This midpoint deformation then leads to an equivalent bending stiffness that effectively accounts for the core shear compliance. Published parametric charts from a honeycomb performance manual^[6] are used to calculate the panel midpoint deformation. Equivalent plate bending stiffness is extracted from the closed-form expression^[7] for deformation under a uniform pressure equated to the computed tray midpoint deformations.

$$D = \frac{0.0444}{12} \frac{qL^4}{(1-\mathbf{n}^2)\mathbf{d}} \quad (\text{A1})$$

where D , q , L , \mathbf{u} , and \mathbf{d} are the plate stiffness parameter, applied pressure, plate length, Poisson ratio, and tray deformation; respectively.

Core density is added to the top and bottom face sheet and payload densities to obtain the total equivalent plate area density (kg/m^2). The bending stiffness, area density, and tray length are then used to calculate modal frequencies^[8]

$$f_{p,n} = \frac{\mathbf{P}}{2} \sqrt{\frac{D}{m}} \left[\left(\frac{p}{L} \right)^2 + \left(\frac{n}{L} \right)^2 \right] \quad (\text{A2})$$

where f is the modal frequency as a function of p and n , m is the area density, and p and n are the number of half waves in any given mode shape.

Appendix B: Closed-Form Calculation of Single-mode Random Vibration Response

A simple oscillator RMS relative displacement response to a flat random base excitation is given in Reference 5. Modification for the response of a single vibration mode to a support structure acceleration PSD, flat (band limited white noise) around the resonant frequency, is given by

$$RMS_{j,n} = \sqrt{\frac{Sf Q \mathbf{j}_j^2 R}{4 \mathbf{w}_n^3}} \quad (B1)$$

where

$RMS_{j,n}$ = root mean square relative displacement response at point j in the n^{th} mode,

Sf = support frame acceleration PSD [(m/sec²)²/Hz],

Q = modal damping factor (reciprocal of twice the critical damping ratio),

\mathbf{j}_j = mode shape amplitude at point of interest,

R = modal participation factor, and

\mathbf{w}_n = resonant frequency for the n th mode (rad/sec).

The modal participation factor is defined as

$$R = \left(\frac{\oint \mathbf{j}^T m d\mathbf{W}}{\oint \mathbf{j}^T m \mathbf{j} d\mathbf{W}} \right)^2 \quad (B2)$$

where m and \mathbf{W} are the mass per unit area and the domain of integration, respectively. For the specific case of a uniform square plate on simple supports, the mode shape function is expressed as

$$\mathbf{j}(x, y) = A \sin\left(\frac{\mathbf{P}x}{L}\right) \sin\left(\frac{\mathbf{P}y}{L}\right), \quad (B3)$$

where A is the arbitrary non-dimensional midpoint amplitude. Upon substitution of (B3) into (B2), the numerator of R becomes

$$\oint \mathbf{j}^T m d\mathbf{W} = mA \int_0^L \int_0^L \sin\left(\frac{\mathbf{P}x}{L}\right) \sin\left(\frac{\mathbf{P}y}{L}\right) dy dx = \frac{4L^2 mA}{\mathbf{P}^2}, \quad (B4)$$

and the denominator of R becomes

$$\oint \mathbf{j}^T m \mathbf{j} d\mathbf{W} = mA^2 \int_0^L \int_0^L \sin^2\left(\frac{\mathbf{P}x}{L}\right) \sin^2\left(\frac{\mathbf{P}y}{L}\right) dy dx = \frac{L^2 mA^2}{4}. \quad (B5)$$

Substitution of (B2), (B4), and (B5) into (B1), where \mathbf{j}_j is equal to A, and replacing \mathbf{w}_n with $2\mathbf{P}f_n$, yields

$$RMS_n = \sqrt{\frac{8SfQ}{\mathbf{P}^7 f_n^3}}. \quad (B6)$$